

On the Volume Conservation of the Immersed Boundary Method

Boyce E. Griffith*

*Leon H. Charney Division of Cardiology, New York University School of Medicine,
550 First Avenue, New York, New York 10016, USA.*

Received 12 January 2011; Accepted (in revised version) 30 September 2011

Available online 20 February 2012

Abstract. The *immersed boundary (IB) method* is an approach to problems of fluid-structure interaction in which an elastic structure is immersed in a viscous incompressible fluid. The IB formulation of such problems uses a Lagrangian description of the structure and an Eulerian description of the fluid. It is well known that some versions of the IB method can suffer from poor volume conservation. Methods have been introduced to improve the volume-conservation properties of the IB method, but they either have been fairly specialized, or have used complex, nonstandard Eulerian finite-difference discretizations. In this paper, we use quasi-static and dynamic benchmark problems to investigate the effect of the choice of Eulerian discretization on the volume-conservation properties of a formally second-order accurate IB method. We consider both collocated and staggered-grid discretization methods. For the tests considered herein, the staggered-grid IB scheme generally yields at least a modest improvement in volume conservation when compared to cell-centered methods, and in many cases considered in this work, the spurious volume changes exhibited by the staggered-grid IB method are more than an order of magnitude smaller than those of the collocated schemes. We also compare the performance of cell-centered schemes that use either exact or approximate projection methods. We find that the volume-conservation properties of approximate projection IB methods depend strongly on the formulation of the projection method. When used with the IB method, we find that pressure-free approximate projection methods can yield extremely poor volume conservation, whereas pressure-increment approximate projection methods yield volume conservation that is nearly identical to that of a cell-centered exact projection method.

AMS subject classifications: 65M06, 65M20, 65R10, 74F10, 76D05

Key words: Immersed boundary method, fluid-structure interaction, collocated discretization, staggered-grid discretization, exact projection method, approximate projection method, volume conservation.

*Corresponding author. *Email address:* boyce.griffith@nyumc.org (B. E. Griffith)

1 Introduction

The *immersed boundary (IB) method* for fluid-structure interaction [1] is a mathematical formulation and numerical scheme for problems in which an elastic structure is immersed in a viscous incompressible fluid. In the IB formulation of such problems, the elasticity of the structure is described in Lagrangian form, and the momentum, velocity, and incompressibility of the coupled fluid-structure system are described in Eulerian form. In the continuous IB formulation, coupling between Lagrangian and Eulerian variables is mediated by integral equations with Dirac delta function kernels. The discrete version of the IB method employs approximations to these integral equations in which a regularized version of the delta function is used in place of the singular delta function kernels. The discretized integral equations are used to *spread* the Lagrangian forces generated by the immersed elastic structure to the Eulerian grid, and to *interpolate* the Eulerian velocity field to the nodes of the Lagrangian mesh.

It is well known that some versions of the IB method can suffer from poor volume conservation [2,3]. This lack of volume conservation manifests itself as an apparent fluid “leak” at fluid-structure interfaces, which occurs even though the Lagrangian structure moves at the local fluid velocity. Peskin and Printz [2] recognized that one cause of this lack of volume conservation is that the interpolated velocity field that determines the motion of the Lagrangian structure is not generally divergence free, even if the Eulerian velocity is divergence free with respect to the discrete divergence operator used in the numerical solution of the incompressible Navier-Stokes equations. To obtain a Lagrangian velocity field that is more nearly incompressible, Peskin and Printz constructed a modified finite-difference approximation to the Eulerian divergence operator that ensures that the interpolated velocity field is divergence free in an average sense. Their *improved volume conservation IB method* [2] uses this modified discretization to dramatically reduce the volume losses exhibited by the standard IB method. Despite the improvements in accuracy offered by this method, it does not appear to be widely used in practice. (See [4–6], however, for recent applications of the method.) A drawback of the improved volume conservation IB method that may have slowed its adoption is that it uses a complex, non-standard finite-difference discretization of the incompressible Navier-Stokes equations. The coefficients of this modified finite-difference scheme must be derived from the form of the regularized delta function, and the resulting finite-difference operators possess broad stencils that can increase the computational expense of the method. Other, more specialized approaches to improving the volume conservation of the IB method have also been introduced, including by Newren [7] and by Stockie [8], but these methods may not be well-suited for general use.

Herein, we study the effect of the Eulerian spatial discretization on the volume conservation of a formally second-order accurate IB method in two spatial dimensions, restricting our attention to standard finite-difference schemes that are similar to discretization methods commonly used in implementations of the IB method. To minimize the differences between the discretization approaches, the Eulerian domain is taken to be periodic

and is discretized using a uniform Cartesian grid. We consider a collocated Eulerian discretization that approximates the pressure and the components of the velocity at the centers of the Cartesian grid cells, and a staggered-grid (i.e., marker-and-cell or MAC [9]) discretization that approximates the pressure at the centers of the Cartesian grid cells, and that approximates the velocity at the centers of the edges of the grid cells. We employ the same second-order accurate, semi-implicit time stepping scheme for both spatial discretizations, and we use nearly identical higher-order upwind discretizations for the convective acceleration term that are based on a version [10] of the piecewise-parabolic method [11].

For the collocated discretization, we solve the incompressible Navier-Stokes equations by either an exact [12–15] or an approximate [16–21] projection method. Exact projection methods ensure that the discrete divergence of the Eulerian velocity field is zero to machine accuracy (when direct solvers are used) or to within the tolerance of the linear solver (when iterative solvers are used). By contrast, approximate projection methods only ensure that the discrete divergence of the Eulerian velocity field is zero to the truncation error of the finite-difference discretization. In practice, exact collocated projection methods may be implemented easily and efficiently only for relatively simple problems, such as those involving uniform grids and periodic boundary conditions, because the exact cell-centered projection operator requires the solution of a discrete Poisson problem with an extended finite-difference stencil and a nontrivial nullspace composed of the so-called checkerboard modes. Approximate projection methods alleviate many of the difficulties of exact projection methods, although they do so at the price of yielding velocity fields that generally are not discretely divergence free. Approximate projection methods have been used with the IB method previously [22–26]; however, to date, there appear to have been few detailed comparisons between IB methods based on exact and approximate projections. Herein, we seek to quantify the extent to which using an approximate projection method affects the volume-conservation properties of the IB method.

Many of the difficulties of exact projection methods for collocated discretizations are not shared by staggered-grid methods. Specifically, exact staggered-grid projection methods require the solution of standard discrete Poisson problems with compact finite-difference stencils. Consequently, unlike collocated schemes, staggered-grid discretizations do not suffer from spurious pressure modes. Moreover, it is straightforward to use staggered-grid schemes for problems with nontrivial physical boundary conditions [27], to develop adaptive staggered discretizations that yield discretely divergence-free velocity fields [28, 29], and to solve the discrete equations via efficient methods like multi-grid [27, 29].

To assess the volume-conservation properties of collocated and staggered-grid IB schemes, we perform quasi-static and dynamic simulations in two spatial dimensions. We consider problems in which a thin interface is immersed in a viscous incompressible fluid, and problems in which a thick elastic body is immersed in fluid. A key contribution of this paper is that it demonstrates that the magnitude of the spurious volume changes generated by the staggered-grid scheme are generally smaller than that of the

collocated methods. For the problems considered in this study that involve sharp jumps in the pressure at fluid-structure interfaces, the staggered-grid IB method yields spurious volume changes that are generally at least one order of magnitude smaller than those generated by the collocated solution methods, and in some cases, the differences between the schemes are even larger.

We also examine the effect on volume conservation of the form of the approximate projection method. We find that pressure-free approximate projection methods, which do not include an approximation to the pressure gradient when solving the momentum equation for an intermediate velocity, can yield extremely poor volume conservation when used with the IB method. By contrast, pressure-increment approximate projection methods, which include a time step-lagged approximation to the pressure gradient when solving the momentum equation, yield volume conservation that is essentially identical to an exact cell-centered projection method.

2 Continuous formulation and numerical methods

2.1 Equations of motion

We provide only a brief overview of the IB method; see [1] for further details. Let $\mathbf{x} = (x_1, x_2) \in V$ denote Cartesian physical coordinates, with V denoting the physical domain; let $\mathbf{s} \in \Omega$ denote Lagrangian (material) coordinates attached to the immersed elastic boundary, with Ω denoting the Lagrangian coordinate domain; and let $\mathbf{X}(\mathbf{s}, t) = (X_1(\mathbf{s}, t), X_2(\mathbf{s}, t)) \in V$ denote the physical position of material point \mathbf{s} at time t . We consider both problems in which the immersed structure is a thin interface, in which case $\Omega \subset \mathbb{R}$ and $\mathbf{s} = s$, and also problems in which the immersed structure is a thick body, in which case $\Omega \subset \mathbb{R}^2$ and $\mathbf{s} = (s_1, s_2)$. The viscosity ν of the fluid is taken to be constant, and the immersed structure is assumed to be massless (in the case of a thin interface) or neutrally buoyant (in the case of a thick body). We remark that although we present the IB equations in dimensional form, our numerical simulations are performed in arbitrary nondimensional units.

The continuous equations of motion for the fluid-structure system are

$$\frac{\partial \mathbf{u}}{\partial t}(\mathbf{x}, t) + \mathbf{u}(\mathbf{x}, t) \cdot \nabla \mathbf{u}(\mathbf{x}, t) = -\nabla p(\mathbf{x}, t) + \nu \nabla^2 \mathbf{u}(\mathbf{x}, t) + \mathbf{f}(\mathbf{x}, t), \quad (2.1)$$

$$\nabla \cdot \mathbf{u}(\mathbf{x}, t) = 0, \quad (2.2)$$

$$\mathbf{f}(\mathbf{x}, t) = \int_{\Omega} \mathbf{F}(\mathbf{s}, t) \delta(\mathbf{x} - \mathbf{X}(\mathbf{s}, t)) d\mathbf{s}, \quad (2.3)$$

$$\mathbf{U}(\mathbf{s}, t) = \int_V \mathbf{u}(\mathbf{x}, t) \delta(\mathbf{x} - \mathbf{X}(\mathbf{s}, t)) d\mathbf{x}, \quad (2.4)$$

$$\frac{\partial \mathbf{X}}{\partial t}(\mathbf{s}, t) = \mathbf{U}(\mathbf{s}, t), \quad (2.5)$$

$$\mathbf{F}(\mathbf{s}, t) = \mathcal{F}[\mathbf{X}(\cdot, t); \mathbf{s}], \quad (2.6)$$

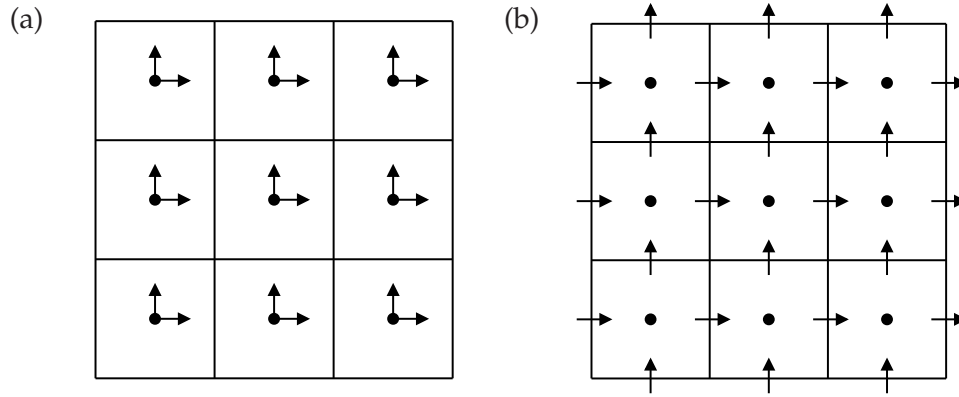


Figure 1: Two Eulerian spatial discretizations. (a) A collocated discretization in which the pressure and the components of the velocity are all defined at the centers of the Cartesian grid cells, i.e., at positions $\mathbf{x}_{i,j} = ((i + \frac{1}{2})h, (j + \frac{1}{2})h)$. (b) A staggered-grid discretization in which the pressure is defined at the centers of the Cartesian grid cells, and the edge-normal components of the velocity are defined at the centers of the edges of the Cartesian grid cells, i.e., at positions $\mathbf{x}_{i-1/2,j} = (ih, (j + \frac{1}{2})h)$ and $\mathbf{x}_{i,j-1/2} = ((i + \frac{1}{2})h, jh)$.

in which $\mathbf{u}(\mathbf{x}, t) = (u_1(\mathbf{x}, t), u_2(\mathbf{x}, t))$ is the Eulerian velocity field, $p(\mathbf{x}, t)$ is the Eulerian pressure, $\mathbf{f}(\mathbf{x}, t) = (f_1(\mathbf{x}, t), f_2(\mathbf{x}, t))$ is the Eulerian elastic force density (i.e., the elastic force density with respect to the physical coordinate system, so that $\mathbf{f}(\mathbf{x}, t) d\mathbf{x}$ has units of force), $\mathbf{F}(\mathbf{s}, t) = (F_1(\mathbf{s}, t), F_2(\mathbf{s}, t))$ is the Lagrangian elastic force density (i.e., the elastic force density with respect to the material coordinate system, so that $\mathbf{F}(\mathbf{s}, t) d\mathbf{s}$ has units of force), $\mathbf{U} = (U_1, U_2)$ is the Lagrangian velocity field, and $\delta(\mathbf{x}) = \delta(x_1)\delta(x_2)$ is the two-dimensional Dirac delta function. We shall describe the form of the Lagrangian elastic force density functional $\mathcal{F} : (\mathbf{X}(\cdot, t), \mathbf{s}) \mapsto \mathbf{F}(\mathbf{s}, t)$ when we introduce the particular benchmark problems considered in this study.

2.2 Eulerian and Lagrangian spatial discretizations

In our computations, the physical domain V is chosen to be the unit square with periodic boundaries and is discretized using a uniform $N \times N$ Cartesian grid, so that the Cartesian grid spacings are $\Delta x_1 = \Delta x_2 = h = \frac{1}{N}$. The Cartesian grid cells are indexed $i, j = 0, 1, \dots, N-1$. The positions of the centers of the Cartesian grid cells are $\mathbf{x}_{i,j} = ((i + \frac{1}{2})h, (j + \frac{1}{2})h)$, and the positions of the centers of the x_1 - and x_2 -edges of the Cartesian grid cells (i.e., the edges $x_1 = \text{constant}$ and $x_2 = \text{constant}$) are, respectively, $\mathbf{x}_{i-1/2,j} = (ih, (j + \frac{1}{2})h)$ and $\mathbf{x}_{i,j-1/2} = ((i + \frac{1}{2})h, jh)$. The collocated schemes approximate the pressure and the components of the velocity at the centers of the Cartesian grid cells, whereas the staggered-grid scheme approximates the pressure at the centers of the Cartesian grid cells and approximates the edge-normal components of the velocity at the centers of the edges of the Cartesian grid cells. See Fig. 1.

Let $\nabla_h \cdot$, ∇_h , and ∇_h^2 denote standard compact second-order accurate finite-difference

approximations to the divergence, gradient, and Laplace operators, respectively (see, e.g., [22, 27] for explicit formulæ for these discrete operators). Notice that in the cell-centered case, $\nabla_h \cdot \nabla_h \neq \nabla_h^2$, whereas in the staggered-grid case, $\nabla_h \cdot \nabla_h = \nabla_h^2$. Specifically, in the cell-centered case, $\nabla_h \cdot \nabla_h$ is similar to the standard five-point finite-difference discretization of the Laplacian, except that it has a broadened stencil that gives rise to a four-dimensional nullspace spanned by the four checkerboard modes. In the staggered-grid case, by contrast, $\nabla_h \cdot \nabla_h$ corresponds to the usual compact five-point Laplacian and possesses a trivial one-dimensional nullspace consisting of grid functions that are constant on the Eulerian grid.

For thin-interface problems, the Lagrangian coordinate space is discretized using a uniform one-dimensional mesh with nodes $\mathbf{s}_k = s_k$ and mesh spacing Δs . For thick-body problems, the Lagrangian coordinate space is discretized using a uniform two-dimensional mesh with nodes $\mathbf{s}_{k,l}$ and mesh spacings Δs_1 and Δs_2 . For simplicity, we shall generally use the two-dimensional Lagrangian notation except when specifically discussing thin-interface examples.

The values $\mathbf{F}_{k,l}$ of the discrete Lagrangian force density associated with node $\mathbf{s}_{k,l}$ are computed from the physical positions $\mathbf{X}_{k,l}$ of the nodes of the Lagrangian mesh via a second-order finite-difference approximation to the Lagrangian force functional \mathcal{F} . In the cell-centered case, the Eulerian force density is determined at the centers of the Cartesian grid cells via

$$\mathbf{f}_{i,j} = \sum_{k,l} \mathbf{F}_{k,l} \delta_h(\mathbf{x}_{i,j} - \mathbf{X}_{k,l}) \Delta s_1 \Delta s_2, \quad (2.7)$$

and in the staggered-grid case, the Eulerian force density is determined at the centers of the edges of the Cartesian grid cells via

$$(f_1)_{i-\frac{1}{2},j} = \sum_{k,l} (F_1)_{k,l} \delta_h(\mathbf{x}_{i-\frac{1}{2},j} - \mathbf{X}_{k,l}) \Delta s_1 \Delta s_2, \quad (2.8)$$

$$(f_2)_{i,j-\frac{1}{2}} = \sum_{k,l} (F_2)_{k,l} \delta_h(\mathbf{x}_{i,j-\frac{1}{2}} - \mathbf{X}_{k,l}) \Delta s_1 \Delta s_2. \quad (2.9)$$

Here, $\delta_h(\mathbf{x}) = \delta_h(x_1) \delta_h(x_2)$ is the two-dimensional regularized delta function, which we define as the tensor product of one-dimensional regularized delta functions. In our computations, we take the one-dimensional delta function $\delta_h(x)$ to be the four-point delta function of Peskin [1]. The motion of the Lagrangian mesh nodes is determined in the cell-centered case via

$$\mathbf{U}_{k,l} = \sum_{i,j} \mathbf{u}_{i,j} \delta_h(\mathbf{x}_{i,j} - \mathbf{X}_{k,l}) h^2, \quad (2.10)$$

and in the staggered-grid case via

$$(U_1)_{k,l} = \sum_{i,j} (u_1)_{i-\frac{1}{2},j} \delta_h(\mathbf{x}_{i-\frac{1}{2},j} - \mathbf{X}_{k,l}) h^2, \quad (2.11)$$

$$(U_2)_{k,l} = \sum_{i,j} (u_2)_{i,j-\frac{1}{2}} \delta_h(\mathbf{x}_{i,j-\frac{1}{2}} - \mathbf{X}_{k,l}) h^2. \quad (2.12)$$

We let $\mathcal{S}[\mathbf{X}]$ denote the discrete *force-spreading* operator, so that $\mathbf{f} = \mathcal{S}[\mathbf{X}]\mathbf{F}$. The corresponding discrete *velocity-interpolation* operator is the adjoint of $\mathcal{S}[\mathbf{X}]$, so that $\mathbf{U} = \mathcal{S}[\mathbf{X}]^* \mathbf{u}$. In the semi-discretized case, choosing the velocity-interpolation operator to be the adjoint of the force-spreading operator ensures that energy is not spuriously created or destroyed during Lagrangian-Eulerian interaction [1].

2.3 Solution methodology

2.3.1 Basic time stepping scheme

We solve the collocated and staggered-grid discretizations of the IB equations of motion via the same semi-implicit, second-order accurate time stepping scheme. Let \mathbf{X}^n , \mathbf{u}^n , and $p^{n-1/2}$ denote the approximations to the values of \mathbf{X} and \mathbf{u} at time $t^n = n\Delta t$, and to the value of p at time $t^{n-1/2} = (n - \frac{1}{2})\Delta t$. To advance \mathbf{X} , \mathbf{u} , and p forward in time by the increment Δt , we first compute \mathbf{X}^{n+1} by a second-order Adams-Bashforth scheme, so that

$$\frac{\mathbf{X}^{n+1} - \mathbf{X}^n}{\Delta t} = \tilde{\mathbf{U}}^{n+\frac{1}{2}}, \quad (2.13)$$

in which

$$\tilde{\mathbf{U}}^{n+\frac{1}{2}} = \frac{3}{2}\mathbf{U}^n - \frac{1}{2}\mathbf{U}^{n-1} \quad \text{and} \quad \mathbf{U}^n = \mathcal{S}[\mathbf{X}^n]^* \mathbf{u}^n. \quad (2.14)$$

We then compute $\mathbf{F}^{n+1/2} = \mathcal{F}[\mathbf{X}^{n+1/2}]$, the intermediate Lagrangian elastic force density corresponding to the intermediate structure configuration

$$\mathbf{X}^{n+\frac{1}{2}} = \frac{1}{2}(\mathbf{X}^{n+1} + \mathbf{X}^n). \quad (2.15)$$

The corresponding intermediate Eulerian elastic force density is $\mathbf{f}^{n+1/2} = \mathcal{S}[\mathbf{X}^{n+1/2}]\mathbf{F}^{n+1/2}$.

Next, we solve the momentum equation,

$$\frac{\mathbf{u}^{n+1,*} - \mathbf{u}^n}{\Delta t} + \tilde{\mathbf{N}}^{n+\frac{1}{2}} = -\nabla_h q^{n+\frac{1}{2}} + \nu \nabla_h^2 \frac{\mathbf{u}^{n+1,*} + \mathbf{u}^n}{2} + \mathbf{f}^{n+\frac{1}{2}}, \quad (2.16)$$

for $\mathbf{u}^{n+1,*}$. Here, $\tilde{\mathbf{N}}^{n+1/2}$ is an explicit, time step-centered approximation to the convective acceleration term $\mathbf{u} \cdot \nabla \mathbf{u}$, and $q^{n+1/2}$ is an explicit approximation to the true time step-centered pressure $p^{n+1/2}$. We describe in Section 2.3.2 the particular choices of $q^{n+1/2}$ used in our numerical experiments. In our computations, $\tilde{\mathbf{N}}^{n+1/2}$ is determined by a second-order Adams-Bashforth method, so that

$$\tilde{\mathbf{N}}^{n+\frac{1}{2}} = \frac{3}{2}\mathbf{N}^n - \frac{1}{2}\mathbf{N}^{n-1}, \quad (2.17)$$

with $\mathbf{N}^n = \mathbf{N}[\mathbf{u}^n]$. Similar methods are used to compute $\mathbf{N}^n = \mathbf{N}[\mathbf{u}^n]$ for the collocated and staggered-grid discretizations, as detailed in Section 2.3.3.

In general, $\mathbf{u}^{n+1,*}$ will not satisfy the discrete divergence-free condition. To obtain an approximation to \mathbf{u} at time t^{n+1} that satisfies (or approximately satisfies) the discrete divergence-free condition, we project (or approximately project) $\mathbf{u}^{n+1,*}$ onto the space of discretely divergence-free vector fields. Specifically, in the case of an exact projection method, we define

$$\mathbf{u}^{n+1} := \left(I - \nabla_h (\nabla_h \cdot \nabla_h)^{-1} \nabla_h \cdot \right) \mathbf{u}^{n+1,*}, \quad (2.18)$$

and in the case of an approximate cell-centered projection method, we define

$$\mathbf{u}^{n+1} := \left(I - \nabla_h (\nabla_h^2)^{-1} \nabla_h \cdot \right) \mathbf{u}^{n+1,*}. \quad (2.19)$$

Notice that the discrete operators $\nabla_h \cdot \nabla_h$ and ∇_h^2 are the same only for the staggered-grid discretization. When these operators differ, the values of \mathbf{u}^{n+1} defined by (2.18) and (2.19) will also generally differ.

For a staggered-grid discretization, the operator $\nabla_h \cdot \nabla_h = \nabla_h^2$ is the usual five-point discrete Laplacian. Thus, the updated velocity fields defined by (2.18) and (2.19) are identical. We refer to the staggered-grid exact projection operator implicitly defined by (2.18) (or, equivalently, by (2.19)) as the *MAC* projection operator. This operator, which maps staggered-grid (MAC) vector fields onto staggered-grid vector fields, is defined by

$$\mathbb{P}_h^{\text{MAC}} = I - \nabla_h (\nabla_h^2)^{-1} \nabla_h \cdot. \quad (2.20)$$

For a collocated discretization, $\nabla_h \cdot \nabla_h \neq \nabla_h^2$. This leads us to distinguish the *exact* cell-centered projection operator,

$$\mathbb{P}_h^{\text{cc}} = I - \nabla_h (\nabla_h \cdot \nabla_h)^{-1} \nabla_h \cdot, \quad (2.21)$$

from the *approximate* cell-centered projection operator,

$$\mathbb{P}_h^{\text{cc},\dagger} = I - \nabla_h (\nabla_h^2)^{-1} \nabla_h \cdot. \quad (2.22)$$

Both \mathbb{P}_h^{cc} and $\mathbb{P}_h^{\text{cc},\dagger}$ map cell-centered vector fields onto cell-centered vector fields. Notice, however, that whereas $\nabla_h \cdot \mathbb{P}_h^{\text{cc}} \mathbf{u}^{n+1,*} = 0$, in general, $\nabla_h \cdot \mathbb{P}_h^{\text{cc},\dagger} \mathbf{u}^{n+1,*} \neq 0$. Instead, $\mathbb{P}_h^{\text{cc},\dagger}$ enforces discrete incompressibility to the truncation error of the finite-difference scheme, i.e., for smooth $\mathbf{u}^{n+1,*}$, $\nabla_h \cdot \mathbb{P}_h^{\text{cc},\dagger} \mathbf{u}^{n+1,*} = \mathcal{O}(h^2)$. See, e.g., [16–23] for further details on approximate projection methods.

The application of the MAC projection operator $\mathbb{P}_h^{\text{MAC}}$, the exact cell-centered projection operator \mathbb{P}_h^{cc} , or the approximate cell-centered projection operator $\mathbb{P}_h^{\text{cc},\dagger}$ requires the solution of a discrete Poisson problem that is of the form

$$L\varphi = \frac{1}{\Delta t} \nabla_h \cdot \mathbf{u}^{n+1,*}, \quad (2.23)$$

in which L is either the operator $\nabla_h \cdot \nabla_h$ for the staggered-grid or exact collocated projection schemes, or the operator ∇_h^2 for the approximate collocated projection schemes. In any case, the solution φ to this discrete Poisson problem is a cell-centered scalar grid function that we use to determine the time step-centered pressure via

$$p^{n+\frac{1}{2}} = q^{n+\frac{1}{2}} + \left(I - \Delta t \frac{\nu}{2} \nabla_h^2 \right) \varphi. \quad (2.24)$$

This pressure-update formula is the second-order accurate pressure update described by Brown, Cortez, and Minion [20].

2.3.2 Choosing $q^{n+\frac{1}{2}}$

Choices for $q^{n+\frac{1}{2}}$ that are commonly used with projection methods include setting $q^{n+\frac{1}{2}} = p^{n-1/2}$, and setting $q^{n+\frac{1}{2}} = 0$. With the former choice, (2.24) becomes

$$p^{n+\frac{1}{2}} = p^{n-\frac{1}{2}} + \left(I - \Delta t \frac{\nu}{2} \nabla_h^2 \right) \varphi, \quad (2.25)$$

so that $\varphi \approx p^{n+1/2} - p^{n-1/2}$. This choice therefore yields a *pressure-increment* projection method. The latter choice results in a *pressure-free* projection method. Our pressure-increment projection method ($q^{n+\frac{1}{2}} = p^{n-1/2}$) is a version of the method of Bell, Colella, and Glaz [15]. In our numerical tests, we use *BCG* to indicate a pressure-increment projection method. Our pressure-free projection method ($q^{n+\frac{1}{2}} = 0$) is similar to the method of Kim and Moin [14], and we use *KM* to identify this solution algorithm.

We remark that for uniform periodic Cartesian grids, because the discrete Eulerian operators commute, it can be shown [27] that the staggered-grid or exact collocated projection method with the second-order pressure update (2.24) is an exact solution method for the coupled system,

$$\frac{\mathbf{u}^{n+1} - \mathbf{u}^n}{\Delta t} + \tilde{\mathbf{N}}^{n+\frac{1}{2}} = -\nabla_h p^{n+\frac{1}{2}} + \nu \nabla_h^2 \frac{\mathbf{u}^{n+1} + \mathbf{u}^n}{2} + \mathbf{f}^{n+\frac{1}{2}}, \quad (2.26)$$

$$\nabla_h \cdot \mathbf{u}^{n+1} = 0. \quad (2.27)$$

In this case, the values of \mathbf{u}^{n+1} and $p^{n+1/2}$ that are determined by the projection method are independent of the choice of $q^{n+1/2}$. In practice, for the exact collocated projection method, we set $q^{n+1/2} = p^{n-1/2}$. For the staggered-grid case, our implementation actually solves (2.26) and (2.27) simultaneously by an iterative Krylov method that uses a version of the staggered-grid projection method as a preconditioner [27]. We emphasize, however, that for uniform periodic grids, like those considered in the present work, this staggered-grid solution methodology yields results that are identical to those of a staggered-grid exact projection method. It is important to note that for the collocated approximate projection method, different choices of $q^{n+1/2}$ will yield different approximations to \mathbf{u}^{n+1} and $p^{n+1/2}$ [18]. We examine the effects of these differences on the accuracy of the IB method in Section 4.

2.3.3 Approximating the convective acceleration term $\mathbf{u} \cdot \nabla \mathbf{u}$

We compute $\mathbf{N} \approx \mathbf{u} \cdot \nabla \mathbf{u}$ in a similar manner for both spatial discretizations. In either case, we define systems of nonoverlapping control volumes that are centered about the components of $\mathbf{u} = (u_1, u_2)$. To compute the m^{th} component of $\mathbf{N} = (N_1, N_2)$, we first determine a staggered-grid advection velocity field $\mathbf{u}^{\text{ADV},m}$ that is defined on the edges of the control volumes associated with component m of the velocity field \mathbf{u} . Next, we use the xsPPM7 variant [10] of the piecewise-parabolic method (PPM) [11] to determine u_m^{PPM} , an upwind-biased interpolation of u_m , on the edges of the control volumes, using $\mathbf{u}^{\text{ADV},m}$ to determine the upwind direction. Finally, for each component m of the velocity field, we evaluate $N_m = \mathbf{u}^{\text{ADV},m} \cdot \nabla_h u_m^{\text{PPM}}$ using second-order compact finite differences. Different control volumes are required for the collocated and staggered-grid discretizations, and this in turn necessitates the use of different advection velocity fields in the two cases.

For the collocated discretization, the control volumes used to compute \mathbf{N} are coincident with the Cartesian grid itself, and the same advection velocity field is used for each component of \mathbf{u} . The single advection velocity field \mathbf{u}^{ADV} is determined by computing the MAC projection of the linear interpolation of \mathbf{u} from the cell centers to the edges of the grid cells. Specifically, we compute

$$(u_1^{\text{ADV},*})_{i+\frac{1}{2},j} = \frac{(u_1)_{i,j} + (u_1)_{i+1,j}}{2}, \quad (2.28)$$

$$(u_2^{\text{ADV},*})_{i,j+\frac{1}{2}} = \frac{(u_2)_{i,j} + (u_2)_{i,j+1}}{2}, \quad (2.29)$$

$$\mathbf{u}^{\text{ADV}} = \mathbb{P}_h^{\text{MAC}} \mathbf{u}^{\text{ADV},*}. \quad (2.30)$$

Notice that, in general, $\mathbf{u}^{\text{ADV}} \neq \mathbf{u}^{\text{ADV},*}$, i.e., the linear interpolation of \mathbf{u} is not generally discretely divergence free, even if $\nabla_h \cdot \mathbf{u} \equiv 0$. We remark that the discrete Poisson problem that must be solved to compute $\mathbf{u}^{\text{ADV}} = \mathbb{P}_h^{\text{MAC}} \mathbf{u}^{\text{ADV},*}$ is precisely the same Poisson problem that must be solved to compute the approximate projection of \mathbf{u}^* . Consequently, for the collocated approximate projection IB method, it is possible to compute \mathbf{u}^{ADV} without solving any additional systems of equations. For the collocated exact-projection IB scheme, however, it is necessary to solve one discrete Poisson problem to obtain \mathbf{u} , and to solve a different discrete Poisson problem to obtain \mathbf{u}^{ADV} .

For the staggered-grid discretization, a different set of control volumes must be used for each component of the velocity field [27]. Specifically, the control volumes associated with the u_1 component of the velocity are obtained by shifting the Cartesian grid by $\frac{1}{2}\Delta x_1 = \frac{1}{2}h$ in the x_1 -coordinate direction, and the control volumes associated with the u_2 component of the velocity are obtained by shifting the Cartesian grid cells by $\frac{1}{2}\Delta x_2 = \frac{1}{2}h$ in the x_2 direction. A different advection velocity field is employed for each system of control volumes. In either case, the advection velocity is simply the linear interpolation of the original staggered-grid velocity field \mathbf{u} to the centers of the edges of the control volumes. For the u_1 component of the velocity, for instance, the corresponding advection

velocity $\mathbf{u}^{\text{ADV},1}$ is determined by

$$(u_1^{\text{ADV},1})_{i,j} = \frac{(u_1)_{i+\frac{1}{2},j} + (u_1)_{i-\frac{1}{2},j}}{2}, \quad (2.31)$$

$$(u_2^{\text{ADV},1})_{i+\frac{1}{2},j+\frac{1}{2}} = \frac{(u_2)_{i,j+\frac{1}{2}} + (u_2)_{i+1,j+\frac{1}{2}}}{2}. \quad (2.32)$$

The advection velocity $\mathbf{u}^{\text{ADV},2}$ corresponding to the u_2 component of the velocity is computed similarly. It is not hard to show that because the staggered-grid velocity field \mathbf{u} is discretely divergence free, the advection velocity field $\mathbf{u}^{\text{ADV},1}$ defined by (2.31) and (2.32) is discretely divergence free with respect to the staggered-grid divergence operator associated with the system of control volumes. In particular,

$$\begin{aligned} (\nabla_h \cdot \mathbf{u}^{\text{ADV},1})_{i+\frac{1}{2},j} &= \frac{(u_1^{\text{ADV},1})_{i+1,j} - (u_1^{\text{ADV},1})_{i,j}}{h} + \frac{(u_2^{\text{ADV},1})_{i+\frac{1}{2},j+\frac{1}{2}} - (u_2^{\text{ADV},1})_{i+\frac{1}{2},j-\frac{1}{2}}}{h} \\ &= \frac{1}{2} \left((\nabla_h \cdot \mathbf{u})_{i,j} + (\nabla_h \cdot \mathbf{u})_{i+1,j} \right) \\ &= 0. \end{aligned} \quad (2.33)$$

A similar argument also shows that $\mathbf{u}^{\text{ADV},2}$ is discretely divergence-free in an analogous sense. Consequently, it is not necessary to solve any additional systems of equations to determine a divergence-free advection velocity field for the staggered-grid scheme.

2.3.4 Initial time step

In the initial time step, we lack values for the time step-lagged quantities \mathbf{U}^{n-1} , \mathbf{N}^{n-1} , and $p^{n-1/2}$ that are needed by our basic time stepping scheme. Consequently, during that initial step, we cannot employ that scheme exactly as described in Section 2.3.1. To obtain a second-order accurate time stepping scheme for the initial time step, we instead solve the equations of motion twice during that time step. For the initial solve, we set $\mathbf{U}^{n-1} = \mathbf{U}^n$, $\mathbf{N}^{n-1} = \mathbf{N}^n$, and $p^{n-1/2} = 0$, and we use the time stepping scheme described previously to compute preliminary approximations $\tilde{\mathbf{X}}^{n+1}$, $\tilde{\mathbf{u}}^{n+1}$, and $\tilde{p}^{n+1/2}$ to the updated structure configuration, velocity, and pressure. Notice that this first solve is essentially a pressure-free projection method along with forward Euler for the nonlinear terms. We then compute final approximations to \mathbf{X} , \mathbf{u} , and p using the time stepping scheme detailed previously, except that we now set

$$\tilde{\mathbf{U}}^{n+1} = \mathcal{S}[\tilde{\mathbf{X}}^{n+1}]^* \tilde{\mathbf{u}}^{n+1}, \quad \tilde{\mathbf{U}}^{n+\frac{1}{2}} = \frac{\tilde{\mathbf{U}}^{n+1} + \mathbf{U}^n}{2}, \quad (2.34)$$

$$\tilde{\mathbf{u}}^{n+\frac{1}{2}} = \frac{\tilde{\mathbf{u}}^{n+1} + \mathbf{u}^n}{2}, \quad \tilde{\mathbf{N}}^{n+\frac{1}{2}} = \mathbf{N}[\tilde{\mathbf{u}}^{n+\frac{1}{2}}], \quad q^{n+\frac{1}{2}} = \tilde{p}^{n+\frac{1}{2}}. \quad (2.35)$$

Notice that this second solve is analogous to using a pressure-increment projection method along with the explicit midpoint rule for the nonlinear terms.

2.4 Implementation

Implementations of the collocated and staggered-grid IB methods are provided by the open-source IBAMR software framework [30], which makes use of the SAMRAI [31–33], PETSc [34–36], and *hypre* [37, 38] libraries. All linear systems of equations are solved via preconditioned Krylov methods with relative convergence thresholds of 1.0e-8.

3 Test problems

We consider both quasi-static and dynamic test problems. For static tests, we use structure configurations and elastic force density functionals that, in the continuous setting, are in static equilibrium. When discretized, these configurations are no longer in equilibrium and therefore induce motion of the fluid-structure system, although the magnitude of these spurious motions converges to zero as we refine the computational grid. The dynamic test problems that we use are perturbed versions of the static cases.

3.1 Thin elastic interfaces

To test the performance of the IB method for problems involving thin elastic interfaces, we set $\Omega = [0, 2\pi]$ with periodic boundary conditions, and we use initial configurations of the form

$$\mathbf{X}(s, t)|_{t=0} = \left(\frac{1}{2} + \alpha \cos(s), \frac{1}{2} + \beta \sin(s) \right), \quad (3.1)$$

which corresponds to a circular or elliptical interface. For the thin-interface tests, we use a Lagrangian elastic force density of the form

$$\mathbf{F}(s, t) = \mathcal{F}[\mathbf{X}(\cdot, t); s] = \kappa \frac{\partial^2 \mathbf{X}}{\partial s^2}(s, t), \quad (3.2)$$

in which κ is a uniform elastic stiffness parameter.

In the static case, we set $\alpha = \beta = \frac{1}{4}$, and in the dynamic case, we set $\alpha = \frac{5}{28}$ and $\beta = \frac{7}{20}$. In either case, the initial configuration of the elastic structure encloses a region with area $\frac{\pi}{16}$. At equilibrium, the structure will enclose a disc of radius $R = \frac{1}{4}$.

We use a uniform Lagrangian mesh with $M = \frac{19}{4} \frac{1}{h}$ nodes, so that the Lagrangian nodes are physically separated by a distance of approximately $\frac{h}{3}$ in the equilibrium configuration. We approximate the Lagrangian force density function using second-order finite differences, which is equivalent to describing the elasticity of the structure in terms of systems of linear springs with zero resting lengths.

3.2 Thick elastic bodies

To test the performance of the IB method for problems involving thick elastic bodies, we set $\Omega = [0, 2\pi] \times [0, w]$ with periodic boundary conditions in the s_1 direction, and we use

initial configurations of the form

$$\mathbf{X}(\mathbf{s}, t)|_{t=0} = \left(\frac{1}{2} + (\alpha + s_2) \cos(s_1), \frac{1}{2} + (\beta + s_2) \sin(s_1) \right), \quad (3.3)$$

which corresponds to a thick circular or elliptical shell. For these tests, we use either a Lagrangian elastic force density that is of the form

$$\mathbf{F}(\mathbf{s}, t) = \mathcal{F}[\mathbf{X}(\cdot, t); \mathbf{s}] = \kappa \frac{\partial^2 \mathbf{X}}{\partial s_1^2}(\mathbf{s}, t), \quad (3.4)$$

or one that is of the form

$$\mathbf{F}(\mathbf{s}, t) = \mathcal{F}[\mathbf{X}(\cdot, t); \mathbf{s}] = \kappa \left(\frac{\partial^2 \mathbf{X}}{\partial s_1^2}(\mathbf{s}, t) + \frac{\partial^2 \mathbf{X}}{\partial s_2^2}(\mathbf{s}, t) \right), \quad (3.5)$$

in which κ is again a uniform elastic stiffness parameter. The former elastic force density corresponds to an elastic shell that is composed of a continuum of circumferential elastic fibers [22, 23, 39, 40], whereas the latter elastic force density corresponds to an elastic shell that is composed of both circumferential and radial fibers [39, 40].

In all cases, we set $w = 0.0625$. In the static case, we set $\alpha = \beta = \frac{1}{4}$, and in the dynamic case, we set $\alpha = \frac{5}{28}$ and $\beta = \frac{7}{20}$. In either case, the initial configuration of the elastic structure encloses a region with area $\frac{\pi}{16}$, and at equilibrium, the structure will enclose a disc of radius $R = \frac{1}{4}$.

We use a uniform Lagrangian mesh with $M_1 = \frac{19}{4} \frac{1}{h}$ nodes in the s_1 coordinate direction and $M_2 = \frac{3}{16} \frac{1}{h} + 1$ nodes in the s_2 coordinate direction, so that the Lagrangian nodes are physically separated by a distance of approximately $\frac{h}{3}$ in the equilibrium configuration. We again approximate the Lagrangian force density function using second-order finite differences, which is equivalent to describing the elasticity of the structure in terms of systems of linear springs with zero resting lengths.

It is interesting to note that the IB method is able to attain second-order convergence rates for the shell that is composed exclusively of circumferential fibers [22, 23, 39, 40], but not for the shell that is composed of both circumferential and radial fibers [39, 40].

4 Numerical experiments

We perform two sets of numerical experiments. In the first set of tests, we use initial configurations that are discretizations of stable equilibrium solutions of the continuous equations. In the second set of computations, we use the same elastic force functions of the quasi-static tests, but we use initial structure configurations that are far from equilibrium. This second set of tests therefore allow us to assess the effects of large nonlinear deformations on volume conservation.

4.1 Quasi-static tests

4.1.1 Thin elastic interface

Our first set of tests uses the equilibrium configuration of the thin elastic interface with the various versions of the IB method. We consider a single value of the boundary stiffness κ along with several choices for the fluid viscosity ν . The Eulerian domain is discretized using a uniform Cartesian grid with $N=64, 128, 256$, or 512 cells in each coordinate direction, the Lagrangian domain is discretized using a corresponding curvilinear mesh, and the time step size is $\Delta t=6.25e-3h$. This choice of time step was approximately

Table 1: Maximum percent area loss for the quasi-static thin-interface test of Section 4.1.1 with $\kappa=1$. The maximum percent area loss is reported for $N=64, 128, 256$, and 512 for the staggered-grid (MAC), cell-centered pressure-increment exact projection (BCG-exact), cell-centered pressure-increment approximate projection (BCG-approx), and cell-centered pressure-free approximate projection (KM-approx) solvers. The minimum and maximum ratios of the cell-centered and staggered-grid results for each value of N are reported in the right two columns. Notice that the staggered-grid scheme yields area losses that are at least a factor of 20 smaller than those yielded by the cell-centered solution methods.

$\kappa=1$											
$\nu=1.0$											
N	MAC	rate	BCG exact	rate	BCG approx	rate	KM approx	rate	min ratio	max ratio	
64	6.67e-4	1.10	1.42e-2	1.01	1.43e-2	1.01	4.96e-1	0.42	2.13e+1	7.44e+2	
128	3.12e-4	0.89	7.09e-3	0.98	7.12e-3	0.99	3.71e-1	0.51	2.27e+1	1.19e+3	
256	1.68e-4	0.83	3.58e-3	0.98	3.59e-3	0.98	2.61e-1	0.59	2.13e+1	1.55e+3	
512	9.45e-5	—	1.82e-3	—	1.82e-3	—	1.73e-1	—	1.93e+1	1.83e+3	
$\nu=1.0e-1$											
N	MAC	rate	BCG exact	rate	BCG approx	rate	KM approx	rate	min ratio	max ratio	
64	5.29e-3	0.95	1.33e-1	0.98	1.33e-1	0.98	9.43e-1	0.24	2.52e+1	1.78e+2	
128	2.73e-3	0.91	6.76e-2	0.96	6.76e-2	0.96	8.00e-1	0.26	2.47e+1	2.93e+2	
256	1.45e-3	0.98	3.48e-2	0.97	3.48e-2	0.97	6.68e-1	0.32	2.39e+1	4.59e+2	
512	7.35e-4	—	1.77e-2	—	1.77e-2	—	5.36e-1	—	2.41e+1	7.30e+2	
$\nu=1.0e-2$											
N	MAC	rate	BCG exact	rate	BCG approx	rate	KM approx	rate	min ratio	max ratio	
64	4.57e-2	0.85	1.21e+0	0.93	1.21e+0	0.93	2.13e+0	0.47	2.64e+1	4.65e+1	
128	2.54e-2	0.92	6.34e-1	0.95	6.34e-1	0.95	1.53e+0	0.36	2.49e+1	6.03e+1	
256	1.35e-2	0.99	3.27e-1	1.02	3.27e-1	1.02	1.20e+0	0.28	2.43e+1	8.87e+1	
512	6.78e-3	—	1.62e-1	—	1.62e-1	—	9.88e-1	—	2.39e+1	1.46e+2	
$\nu=1.0e-3$											
N	MAC	rate	BCG exact	rate	BCG approx	rate	KM approx	rate	min ratio	max ratio	
64	2.60e-1	0.49	6.40e+0	0.50	6.40e+0	0.50	7.27e+0	0.40	2.46e+1	2.80e+1	
128	1.85e-1	0.91	4.54e+0	0.82	4.54e+0	0.82	5.50e+0	0.62	2.45e+1	2.97e+1	
256	9.86e-2	1.13	2.57e+0	1.05	2.57e+0	1.05	3.58e+0	0.67	2.61e+1	3.63e+1	
512	4.50e-2	—	1.24e+0	—	1.24e+0	—	2.24e+0	—	2.76e+1	4.99e+1	

Table 2: Rate of area loss for the quasi-static thin-interface test of Section 4.1.1 with $\kappa=1$. The rate of area loss is reported for $N=64, 128, 256,$ and 512 for the staggered-grid (MAC), cell-centered pressure-increment exact projection (BCG-exact), cell-centered pressure-increment approximate projection (BCG-approx), and cell-centered pressure-free approximate projection (KM-approx) solvers. The minimum and maximum ratios of the cell-centered and staggered-grid results for each value of N are reported in the right two columns. Notice that the staggered-grid scheme yields rates of area loss that are at least a factor of 20 smaller than those yielded by the cell-centered solution methods.

$\kappa=1$										
$\nu=1.0$										
N	MAC	rate	BCG exact	rate	BCG approx	rate	KM approx	rate	min ratio	max ratio
64	2.08e-6	0.92	5.09e-5	1.01	5.09e-5	1.01	1.77e-3	0.42	2.44e+1	8.50e+2
128	1.10e-6	1.06	2.53e-5	0.98	2.53e-5	0.98	1.32e-3	0.51	2.29e+1	1.20e+3
256	5.30e-7	0.91	1.28e-5	0.99	1.28e-5	0.99	9.32e-4	0.59	2.42e+1	1.76e+3
512	2.82e-7	—	6.45e-6	—	6.45e-6	—	6.18e-4	—	2.28e+1	2.19e+3
$\nu=1.0e-1$										
N	MAC	rate	BCG exact	rate	BCG approx	rate	KM approx	rate	min ratio	max ratio
64	1.86e-5	0.93	4.74e-4	0.98	4.74e-4	0.98	3.36e-3	0.24	2.55e+1	1.81e+2
128	9.77e-6	0.93	2.41e-4	0.96	2.41e-4	0.96	2.86e-3	0.26	2.46e+1	2.92e+2
256	5.14e-6	0.97	1.24e-4	0.97	1.24e-4	0.97	2.39e-3	0.32	2.41e+1	4.64e+2
512	2.62e-6	—	6.31e-5	—	6.31e-5	—	1.91e-3	—	2.41e+1	7.30e+2
$\nu=1.0e-2$										
N	MAC	rate	BCG exact	rate	BCG approx	rate	KM approx	rate	min ratio	max ratio
64	1.68e-4	0.87	4.42e-3	0.95	4.42e-3	0.95	7.70e-3	0.48	2.63e+1	4.58e+1
128	9.21e-5	0.92	2.29e-3	0.96	2.29e-3	0.96	5.50e-3	0.36	2.49e+1	5.98e+1
256	4.85e-5	1.00	1.18e-3	1.02	1.18e-3	1.02	4.28e-3	0.28	2.42e+1	8.81e+1
512	2.42e-5	—	5.78e-4	—	5.78e-4	—	3.52e-3	—	2.39e+1	1.45e+2
$\nu=1.0e-3$										
N	MAC	rate	BCG exact	rate	BCG approx	rate	KM approx	rate	min ratio	max ratio
64	9.89e-4	0.51	2.45e-2	0.54	2.45e-2	0.54	2.77e-2	0.45	2.48e+1	2.80e+1
128	6.95e-4	0.95	1.68e-2	0.86	1.68e-2	0.86	2.02e-2	0.65	2.42e+1	2.91e+1
256	3.59e-4	1.18	9.27e-3	1.07	9.27e-3	1.07	1.29e-2	0.68	2.59e+1	3.59e+1
512	1.58e-4	—	4.42e-3	—	4.42e-3	—	8.02e-3	—	2.80e+1	5.07e+1

the largest that resulted in stable computations for the range of material and numerical parameters considered in this study.

Because the immersed structure is initialized in a configuration that is a discretization of an equilibrium configuration of the continuous equations, we consider any motion of the structure or change in the area enclosed by the structure to constitute an error in the computed solution. To assess such errors in volume conservation, we track the area enclosed by the interface over the time interval $t \in [0,0.55]$, which corresponds to approximately a single period in the dynamic case. The maximum percent change in area is reported in Table 1 for the various solution algorithms and material and numerical parameters. The rates of area loss are also computed by linear regression from these time-dependent data, and the results are reported in Table 2.

For these tests, the staggered-grid scheme yields area losses that are generally at least a factor of 20 smaller than those produced by the exact or pressure-increment approximate projection methods, and that are one to two orders of magnitude smaller than those generated by the pressure-free approximate projection scheme. Similar differences are seen in the rate of area loss, with the staggered-grid scheme yielding significantly smaller rates of area change than the collocated schemes. Notice that the staggered-grid and pressure-increment collocated projection schemes all appear to be converging at a first-order rate, whereas the pressure-free collocated projection method appears to be converging at a sublinear rate. Also notice that the exact and approximate pressure-increment projection methods yield essentially identical results.

4.1.2 Elastic shell composed of circumferential fibers

Our next set of tests uses the equilibrium configuration of the thick elastic shell that is composed of only circumferential fibers. Unlike the test of Section 4.1.1, in this case, the immersed structure is a thick elastic body, and because all of the fibers that compose the structure are periodic, the elastic forces generated by the structure do not produce any discontinuities in the pressure.

We consider a single value of the boundary stiffness κ along with several choices for the fluid viscosity ν . The Eulerian domain is discretized using a uniform Cartesian grid with $N = 64, 128, 256, \text{ or } 512$ cells in each coordinate direction, the Lagrangian domain is discretized using a corresponding curvilinear mesh, and the time step size is $\Delta t = 2.34375e-2h$. This choice of time step was approximately the largest that resulted in stable computations for the range of material and numerical parameters considered in this study.

Because the immersed structure is initialized in a configuration that is a discretization of an equilibrium configuration of the continuous equations, we consider any motion of the structure or change in the area enclosed by the structure to constitute an error in the computed solution. To assess such errors, we track the area of the thick shell over the time interval $t \in [0, 0.703125]$, which corresponds to approximately a single period in the dynamic problem. The maximum percent change in area is reported in Table 3 for the various solution algorithms and material and numerical parameters. The rates of area loss are also computed by linear regression from these time-dependent data, and the results are reported in Table 4. Notice that in some cases, the staggered-grid scheme does not yield a loss of area but rather a small gain in area.

This test yields essentially second-order convergence rates for each of the numerical methods in most cases. All methods yield area changes of less than 1%, and the staggered-grid scheme yields area changes of less than 0.01%. Except for the case in which $\nu=1.0$, the staggered-grid scheme yields area changes that are at least a factor of 10–20 smaller than those produced by the exact or pressure-increment approximate projection methods. The comparatively slow convergence rates observed for $\nu=1.0$ are the result of finite-precision effects. Higher-order convergence rates are observed when we use linear solvers with tighter convergence thresholds (data not shown). Notice, how-

Table 3: Maximum percent area loss for the quasi-static elastic-shell test of Section 4.1.2 with $\kappa=1$. The maximum percent area loss is reported for $N=64, 128, 256,$ and 512 for the staggered-grid (MAC), cell-centered pressure-increment exact projection (BCG-exact), cell-centered pressure-increment approximate projection (BCG-approx), and cell-centered pressure-free approximate projection (KM-approx) solvers. The minimum and maximum ratios of the cell-centered and staggered-grid results for each value of N are reported in the right two columns. Except for the case in which $\nu=1.0$, the staggered-grid scheme yields area losses that are at least a factor of 10-20 smaller than those produced by the cell-centered schemes. For $\nu=1.0$, finite-precision effects are dominating the results. Higher-order convergence rates can be obtained by using a tighter convergence threshold for the iterative linear solvers.

$\kappa=1$											
$\nu=1.0$											
N	MAC	rate	BCG exact	rate	BCG approx	rate	KM approx	rate	min ratio	max ratio	
64	6.79e-5	1.96	1.17e-3	2.75	1.26e-3	2.78	2.51e-1	2.12	1.73e+1	3.70e+3	
128	1.74e-5	2.51	1.74e-4	2.93	1.83e-4	2.94	5.80e-2	2.24	1.00e+1	3.33e+3	
256	-3.05e-6	0.41	2.29e-5	2.91	2.39e-5	2.95	1.23e-2	2.31	7.54e+0	4.03e+3	
512	-2.29e-6	—	3.05e-6	—	3.08e-6	—	2.47e-3	—	1.33e+0	1.08e+3	
$\nu=1.0e-1$											
N	MAC	rate	BCG exact	rate	BCG approx	rate	KM approx	rate	min ratio	max ratio	
64	4.24e-4	2.36	8.24e-3	2.54	8.35e-3	2.54	3.70e-1	2.00	1.94e+1	8.72e+2	
128	8.24e-5	2.72	1.42e-3	2.74	1.43e-3	2.75	9.21e-2	2.10	1.72e+1	1.12e+3	
256	1.25e-5	2.65	2.12e-4	2.86	2.13e-4	2.86	2.16e-2	2.17	1.70e+1	1.72e+3	
512	-1.99e-6	—	2.92e-5	—	2.94e-5	—	4.80e-3	—	1.47e+1	2.42e+3	
$\nu=1.0e-2$											
N	MAC	rate	BCG exact	rate	BCG approx	rate	KM approx	rate	min ratio	max ratio	
64	2.44e-3	2.22	5.15e-2	2.32	5.16e-2	2.32	4.52e-1	1.96	2.11e+1	1.85e+2	
128	5.25e-4	2.52	1.03e-2	2.56	1.04e-2	2.56	1.16e-1	2.03	1.97e+1	2.22e+2	
256	9.15e-5	2.86	1.75e-3	2.75	1.75e-3	2.75	2.86e-2	2.07	1.92e+1	3.12e+2	
512	1.26e-5	—	2.61e-4	—	2.61e-4	—	6.81e-3	—	2.07e+1	5.41e+2	
$\nu=1.0e-3$											
N	MAC	rate	BCG exact	rate	BCG approx	rate	KM approx	rate	min ratio	max ratio	
64	8.44e-3	1.98	1.62e-1	2.01	1.62e-1	2.01	5.79e-1	1.94	1.92e+1	6.86e+1	
128	2.14e-3	2.21	4.04e-2	2.22	4.05e-2	2.22	1.51e-1	2.03	1.89e+1	7.08e+1	
256	4.62e-4	2.43	8.70e-3	2.47	8.70e-3	2.47	3.71e-2	2.09	1.88e+1	8.04e+1	
512	8.57e-5	—	1.57e-3	—	1.57e-3	—	8.72e-3	—	1.83e+1	1.02e+2	

ever, that for $\nu=1.0$, the staggered-grid scheme yields area losses that are smaller than 0.0001%. For all values of ν considered, the staggered-grid scheme also yields volume changes that are one to three orders of magnitude smaller than those generated by the pressure-free approximate projection scheme. The differences in the rate of area change are similar, with the staggered-grid scheme yielding superior results in all cases considered. As before, the exact and approximate pressure-increment projection methods yield essentially identical results.

Table 4: Rate of area loss for the quasi-static elastic-shell test of Section 4.1.2 with $\kappa=1$. The rate of area loss is reported for $N=64, 128, 256$, and 512 for the staggered-grid (MAC), cell-centered pressure-increment exact projection (BCG-exact), cell-centered pressure-increment approximate projection (BCG-approx), and cell-centered pressure-free approximate projection (KM-approx) solvers. The minimum and maximum ratios of the cell-centered and staggered-grid results for each value of N are reported in the right two columns. The staggered-grid scheme yields rates of area loss that are generally at least a factor of 10-20 smaller than those produced by the cell-centered schemes.

$\kappa=1$										
$\nu=1.0$										
N	MAC	rate	BCG exact	rate	BCG approx	rate	KM approx	rate	min ratio	max ratio
64	3.07e-6	1.24	5.38e-5	1.84	5.37e-5	1.84	1.16e-2	1.17	1.75e+1	3.78e+3
128	1.30e-6	1.75	1.50e-5	1.97	1.50e-5	1.96	5.15e-3	1.27	1.15e+1	3.96e+3
256	3.85e-7	1.36	3.85e-6	1.16	3.86e-6	1.17	2.13e-3	1.33	9.98e+0	5.54e+3
512	1.50e-7	—	1.73e-6	—	1.72e-6	—	8.51e-4	—	1.15e+1	5.67e+3
$\nu=1.0e-1$										
N	MAC	rate	BCG exact	rate	BCG approx	rate	KM approx	rate	min ratio	max ratio
64	1.84e-5	1.46	3.71e-4	1.58	3.72e-4	1.58	1.71e-2	1.06	2.02e+1	9.29e+2
128	6.67e-6	1.48	1.25e-4	1.78	1.24e-4	1.78	8.18e-3	1.13	1.87e+1	1.23e+3
256	2.39e-6	2.62	3.62e-5	1.84	3.62e-5	1.84	3.75e-3	1.18	1.51e+1	1.57e+3
512	3.90e-7	—	1.01e-5	—	1.01e-5	—	1.65e-3	—	2.59e+1	4.24e+3
$\nu=1.0e-2$										
N	MAC	rate	BCG exact	rate	BCG approx	rate	KM approx	rate	min ratio	max ratio
64	1.14e-4	1.30	2.41e-3	1.38	2.41e-3	1.38	2.09e-2	1.02	2.11e+1	1.83e+2
128	4.65e-5	1.52	9.25e-4	1.59	9.25e-4	1.59	1.03e-2	1.06	1.99e+1	2.22e+2
256	1.62e-5	1.97	3.07e-4	1.77	3.07e-4	1.77	4.97e-3	1.08	1.90e+1	3.07e+2
512	4.14e-6	—	8.98e-5	—	8.98e-5	—	2.34e-3	—	2.17e+1	5.65e+2
$\nu=1.0e-3$										
N	MAC	rate	BCG exact	rate	BCG approx	rate	KM approx	rate	min ratio	max ratio
64	4.20e-4	1.10	7.96e-3	1.12	7.96e-3	1.12	2.72e-2	1.01	1.90e+1	6.48e+1
128	1.96e-4	1.26	3.65e-3	1.27	3.65e-3	1.27	1.35e-2	1.06	1.86e+1	6.88e+1
256	8.17e-5	1.48	1.52e-3	1.49	1.52e-3	1.49	6.47e-3	1.11	1.86e+1	7.92e+1
512	2.92e-5	—	5.39e-4	—	5.39e-4	—	3.00e-3	—	1.84e+1	1.03e+2

4.1.3 Elastic shell composed of circumferential and radial fibers

Our final set of quasi-static tests uses the equilibrium configuration of the thick elastic shell that is composed of both circumferential and radial fibers. An important difference between this case and that of Section 4.1.2 is that the radial fibers that terminate at the fluid-structure interface generate a discontinuity in the pressure at that interface.

We consider a single value of the boundary stiffness κ along with several choices for the fluid viscosity ν . The Eulerian domain is discretized using a uniform Cartesian grid with $N=64, 128, 256$, or 512 cells in each coordinate direction, the Lagrangian domain is discretized using a corresponding curvilinear mesh, and the time step size is

Table 5: Maximum percent area loss for the quasi-static elastic-shell test of Section 4.1.3 with $\kappa=1$. The maximum percent area loss is reported for $N=64, 128, 256,$ and 512 for the staggered-grid (MAC), cell-centered pressure-increment exact projection (BCG-exact), cell-centered pressure-increment approximate projection (BCG-approx), and cell-centered pressure-free approximate projection (KM-approx) solvers. The minimum and maximum ratios of the cell-centered and staggered-grid results for each value of N are reported in the right two columns. The staggered-grid scheme yields area losses that are at least a factor of 10-30 smaller than those produced by the cell-centered schemes.

$\kappa=1$										
$\nu=1.0$										
N	MAC	rate	BCG exact	rate	BCG approx	rate	KM approx	rate	min ratio	max ratio
64	1.37e-2	0.99	3.96e-1	1.16	4.07e-1	1.17	3.86e+1	0.95	2.90e+1	2.83e+3
128	6.88e-3	0.90	1.78e-1	0.98	1.81e-1	0.99	2.00e+1	0.81	2.58e+1	2.90e+3
256	3.70e-3	0.96	9.02e-2	0.98	9.12e-2	0.99	1.14e+1	0.75	2.44e+1	3.08e+3
512	1.91e-3	—	4.57e-2	—	4.60e-2	—	6.76e+0	—	2.40e+1	3.55e+3
$\nu=1.0e-1$										
N	MAC	rate	BCG exact	rate	BCG approx	rate	KM approx	rate	min ratio	max ratio
64	7.03e-2	0.86	1.89e+0	1.00	1.91e+0	1.01	6.85e+1	0.71	2.69e+1	9.75e+2
128	3.87e-2	0.93	9.43e-1	1.04	9.52e-1	1.04	4.19e+1	0.72	2.43e+1	1.08e+3
256	2.04e-2	0.94	4.59e-1	0.99	4.63e-1	0.99	2.54e+1	0.58	2.25e+1	1.25e+3
512	1.06e-2	—	2.31e-1	—	2.32e-1	—	1.70e+1	—	2.18e+1	1.61e+3
$\nu=1.0e-2$										
N	MAC	rate	BCG exact	rate	BCG approx	rate	KM approx	rate	min ratio	max ratio
64	2.13e-1	0.79	3.31e+0	0.84	3.34e+0	0.84	7.95e+1	0.44	1.56e+1	3.73e+2
128	1.23e-1	0.93	1.85e+0	0.98	1.87e+0	0.98	5.84e+1	0.71	1.50e+1	4.73e+2
256	6.47e-2	0.96	9.43e-1	1.00	9.49e-1	1.00	3.58e+1	0.44	1.46e+1	5.53e+2
512	3.33e-2	—	4.70e-1	—	4.73e-1	—	2.63e+1	—	1.41e+1	7.91e+2
$\nu=1.0e-3$										
N	MAC	rate	BCG exact	rate	BCG approx	rate	KM approx	rate	min ratio	max ratio
64	4.22e-1	0.95	4.52e+0	1.09	4.54e+0	1.09	8.49e+1	0.34	1.07e+1	2.01e+2
128	2.19e-1	0.97	2.12e+0	0.96	2.13e+0	0.96	6.72e+1	0.71	9.68e+0	3.07e+2
256	1.12e-1	0.98	1.09e+0	0.99	1.10e+0	0.99	4.10e+1	0.39	9.76e+0	3.67e+2
512	5.66e-2	—	5.48e-1	—	5.51e-1	—	3.13e+1	—	9.68e+0	5.53e+2

$\Delta t = 2.34375e-2h$. This choice of time step was approximately the largest that resulted in stable computations for the range of material and numerical parameters considered in this study.

Because the immersed structure is initialized in a configuration that is a discretization of an equilibrium configuration of the continuous equations, we consider any motion of the structure or change in the area enclosed by the structure to constitute an error in the computed solution. To assess such errors, we track the area of the thick shell over the time interval $t \in [0, 1.40625]$, which corresponds to approximately a single period in the dynamic problem. The maximum percent change in area is reported in Table 5 for the various solution algorithms and material and numerical parameters. The rates of area

Table 6: Rate of area loss for the quasi-static elastic-shell test of Section 4.1.3 with $\kappa=1$. The rate of area loss is reported for $N=64, 128, 256$, and 512 for the staggered-grid (MAC), cell-centered pressure-increment exact projection (BCG-exact), cell-centered pressure-increment approximate projection (BCG-approx), and cell-centered pressure-free approximate projection (KM-approx) solvers. The minimum and maximum ratios of the cell-centered and staggered-grid results for each value of N are reported in the right two columns. The staggered-grid scheme yields rates of area loss that are at least a factor of three smaller than those produced by the cell-centered schemes, with the smallest differences occurring for the smallest viscosities. For larger viscosities, the staggered-grid scheme yields rates of area loss that are at least a factor of 10 smaller than those of the cell-centered methods.

$\kappa=1$										
$\nu=1.0$										
N	MAC	rate	BCG exact	rate	BCG approx	rate	KM approx	rate	min ratio	max ratio
64	1.03e-5	0.99	3.02e-4	1.16	3.02e-4	1.16	3.03e-2	0.97	2.94e+1	2.95e+3
128	5.19e-6	0.90	1.35e-4	0.97	1.35e-4	0.97	1.54e-2	0.81	2.60e+1	2.97e+3
256	2.78e-6	0.94	6.89e-5	0.98	6.90e-5	0.98	8.78e-3	0.75	2.48e+1	3.16e+3
512	1.45e-6	—	3.51e-5	—	3.51e-5	—	5.20e-3	—	2.43e+1	3.60e+3
$\nu=1.0e-1$										
N	MAC	rate	BCG exact	rate	BCG approx	rate	KM approx	rate	min ratio	max ratio
64	5.14e-5	0.84	1.37e-3	0.98	1.37e-3	0.98	5.44e-2	0.81	2.66e+1	1.06e+3
128	2.88e-5	0.94	6.94e-4	1.06	6.93e-4	1.06	3.10e-2	0.74	2.41e+1	1.08e+3
256	1.50e-5	0.95	3.33e-4	0.99	3.33e-4	0.99	1.86e-2	0.59	2.23e+1	1.24e+3
512	7.77e-6	—	1.68e-4	—	1.68e-4	—	1.24e-2	—	2.16e+1	1.59e+3
$\nu=1.0e-2$										
N	MAC	rate	BCG exact	rate	BCG approx	rate	KM approx	rate	min ratio	max ratio
64	1.37e-4	0.79	1.45e-3	0.72	1.45e-3	0.72	6.19e-2	0.53	1.06e+1	4.52e+2
128	7.90e-5	0.94	8.77e-4	0.92	8.77e-4	0.92	4.28e-2	0.75	1.11e+1	5.42e+2
256	4.11e-5	0.97	4.62e-4	1.02	4.63e-4	1.02	2.54e-2	0.45	1.12e+1	6.18e+2
512	2.10e-5	—	2.28e-4	—	2.28e-4	—	1.86e-2	—	1.09e+1	8.84e+2
$\nu=1.0e-3$										
N	MAC	rate	BCG exact	rate	BCG approx	rate	KM approx	rate	min ratio	max ratio
64	2.55e-4	1.29	1.39e-3	2.01	1.39e-3	2.00	6.46e-2	0.40	5.43e+0	2.53e+2
128	1.04e-4	1.10	3.46e-4	1.05	3.46e-4	1.05	4.90e-2	0.78	3.31e+0	4.70e+2
256	4.86e-5	1.06	1.67e-4	1.01	1.67e-4	1.01	2.86e-2	0.39	3.43e+0	5.88e+2
512	2.34e-5	—	8.28e-5	—	8.28e-5	—	2.17e-2	—	3.54e+0	9.30e+2

loss are also computed by linear regression from these time-dependent data, and the results are reported in Table 6. Notice that in some cases, the staggered-grid scheme does not yield a loss of area but rather a small gain in area.

This test yields essentially first-order convergence rates for the staggered-grid and pressure-increment projection methods, whereas the pressure-free approximate projection method yields sublinear convergence rates. Although the staggered-grid and collocated pressure-increment schemes yield area changes that are relatively small, the pressure-free approximate projection method generates a large loss of area, with area

losses of nearly 90% in some cases. As before, the staggered-grid scheme yields the lowest area losses and rates of area change, and the exact and approximate pressure-increment projection methods yield essentially identical results.

4.2 Dynamic tests

4.2.1 Thin elastic interface

Our first set of dynamic tests uses the nonequilibrium configuration of the thin elastic interface with the various versions of the IB method. Upon release at the beginning of

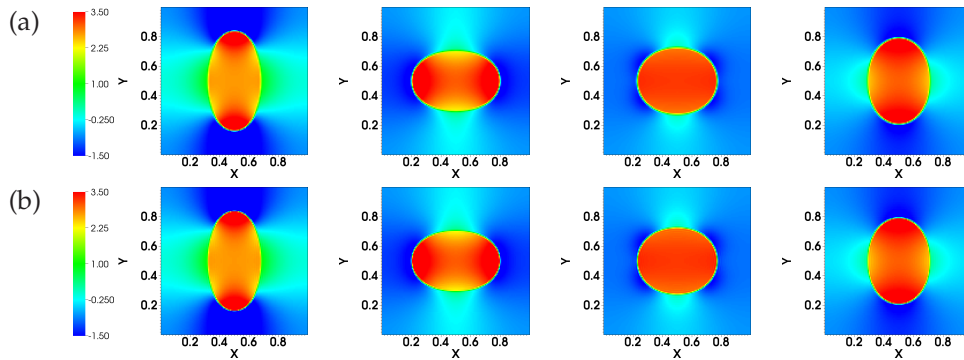


Figure 2: Results from the dynamic thin-interface test of Section 4.2.1. The top panels (a) show the pressure generated by the staggered-grid scheme at equally spaced time intervals during the first oscillation. The bottom panels (b) show the corresponding pressures generated by the pressure-increment approximate projection method. In both cases, $N=128$, $\nu=1.0e-2$, and $\kappa=1$.

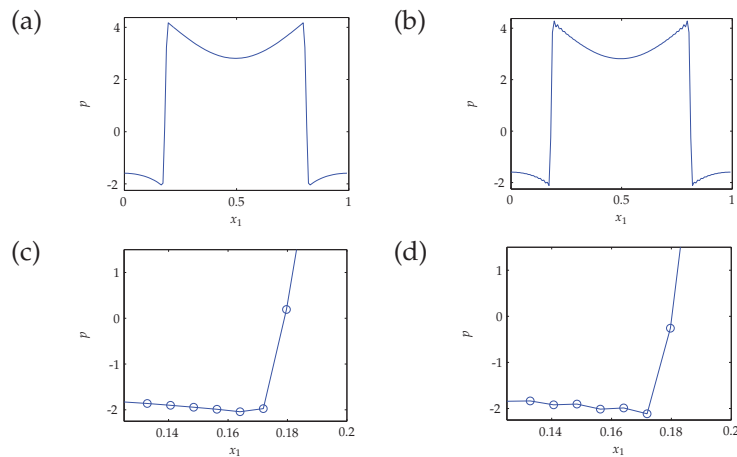


Figure 3: Pressure along $x_2=0.5$ for the staggered-grid (a and c) and pressure-increment approximate projection (b and d) IB methods for the dynamic thin-interface test of Section 4.2.1. Although both schemes regularize discontinuities in the pressure, notice the comparatively sharp resolution of the pressure discontinuity produced by the staggered-grid scheme. By contrast, the collocated scheme generates significant nonphysical pressure oscillations in the vicinity of such discontinuities.

Table 7: Maximum percent area loss (or gain) for the dynamic thin-interface test of Section 4.2.1 with $\nu=1.0e-2$. The maximum percent area loss (or gain) is reported for $N=64, 128, 256,$ and 512 for the staggered-grid (MAC), cell-centered pressure-increment exact projection (BCG-exact), cell-centered pressure-increment approximate projection (BCG-approx), and cell-centered pressure-free approximate projection (KM-approx) solvers. The minimum and maximum ratios of the cell-centered and staggered-grid results for each value of N are reported in the right two columns. The staggered-grid scheme yields changes in area that are generally at least a factor of 10-20 smaller than those produced by the cell-centered schemes. The differences between the discretization methods appear to increase with the elastic stiffness coefficient κ .

$\nu=1.0e-2$											
$\kappa=0.1$											
N	MAC	rate	BCG exact	rate	BCG approx	rate	KM approx	rate	min ratio	max ratio	
64	-7.25e-2	1.05	8.40e-1	0.90	8.40e-1	0.90	3.64e+0	0.22	1.16e+1	5.02e+1	
128	-3.52e-2	1.06	4.49e-1	0.89	4.49e-1	0.89	3.13e+0	0.20	1.28e+1	8.91e+1	
256	-1.69e-2	1.04	2.42e-1	0.93	2.42e-1	0.93	2.74e+0	0.22	1.43e+1	1.62e+2	
512	-8.20e-3	—	1.27e-1	—	1.27e-1	—	2.35e+0	—	1.55e+1	2.87e+2	
$\kappa=1$											
N	MAC	rate	BCG exact	rate	BCG approx	rate	KM approx	rate	min ratio	max ratio	
64	-1.90e-1	1.01	2.22e+0	0.80	2.22e+0	0.80	4.97e+0	0.32	1.17e+1	2.62e+1	
128	-9.40e-2	1.06	1.27e+0	0.84	1.27e+0	0.84	3.97e+0	0.25	1.35e+1	4.22e+1	
256	-4.51e-2	1.05	7.12e-1	0.91	7.12e-1	0.91	3.33e+0	0.22	1.58e+1	7.39e+1	
512	-2.17e-2	—	3.79e-1	—	3.79e-1	—	2.86e+0	—	1.74e+1	1.32e+2	
$\kappa=10$											
N	MAC	rate	BCG exact	rate	BCG approx	rate	KM approx	rate	min ratio	max ratio	
64	-3.08e-1	0.70	4.89e+0	0.53	4.89e+0	0.53	7.48e+0	0.32	1.59e+1	2.43e+1	
128	-1.90e-1	0.96	3.39e+0	0.73	3.39e+0	0.73	5.97e+0	0.37	1.78e+1	3.15e+1	
256	-9.76e-2	1.05	2.04e+0	0.85	2.04e+0	0.85	4.62e+0	0.33	2.09e+1	4.73e+1	
512	-4.73e-2	—	1.14e+0	—	1.14e+0	—	3.67e+0	—	2.41e+1	7.75e+1	
$\kappa=100$											
N	MAC	rate	BCG exact	rate	BCG approx	rate	KM approx	rate	min ratio	max ratio	
64	-2.39e-1	0.20	8.18e+0	0.06	8.18e+0	0.06	1.05e+1	0.04	3.41e+1	4.40e+1	
128	-2.08e-1	0.72	7.87e+0	0.48	7.87e+0	0.48	1.02e+1	0.34	3.78e+1	4.92e+1	
256	-1.27e-1	1.05	5.65e+0	0.71	5.65e+0	0.71	8.07e+0	0.46	4.46e+1	6.37e+1	
512	-6.12e-2	—	3.45e+0	—	3.45e+0	—	5.87e+0	—	5.64e+1	9.60e+1	

the simulations, the elastic interface undergoes damped oscillations. We empirically determined that the duration of the first oscillation is approximately $\frac{3.0625 \log_{10}(\kappa)}{\kappa} 0.55$ for the range of boundary stiffnesses considered. We perform simulations similar to those of Section 4.1.1, except that here we allow the perturbed structure to undergo approximately three damped oscillations. Sample simulation results are shown in Figs. 2 and 3. Detailed results for $N=64, 128, 256,$ and 512 are reported in Tables 7 and 8 for $\nu=1.0e-2$ and for $\kappa=0.1, 1, 10,$ and 100 . Notice that an increase in the elastic stiffness coefficient also has the effect of increasing the Reynolds number of the flow. The staggered-grid scheme yields changes in area that are generally at least a factor of 10–20 smaller than those produced

Table 8: Rate of area loss (gain) for the dynamic thin-interface test of Section 4.2.1 with $\nu=1.0e-2$. The rate of area loss (gain) is reported for $N=64, 128, 256,$ and 512 for the staggered-grid (MAC), cell-centered pressure-increment exact projection (BCG-exact), cell-centered pressure-increment approximate projection (BCG-approx), and cell-centered pressure-free approximate projection (KM-approx) solvers. The minimum and maximum ratios of the cell-centered and staggered-grid results for each value of N are reported in the right two columns. The staggered-grid scheme yields rates of area change that are one to two orders of magnitude smaller than those yielded by the cell-centered solution methods.

$\nu=1.0e-2$										
$\kappa=0.1$										
N	MAC	rate	BCG exact	rate	BCG approx	rate	KM approx	rate	min ratio	max ratio
64	1.58e-6	-0.39	3.80e-4	0.91	3.80e-4	0.91	1.40e-3	0.25	2.40e+2	8.85e+2
128	2.08e-6	0.37	2.03e-4	0.91	2.03e-4	0.91	1.18e-3	0.22	9.75e+1	5.68e+2
256	1.61e-6	0.68	1.08e-4	0.94	1.08e-4	0.94	1.02e-3	0.23	6.71e+1	6.31e+2
512	1.01e-6	—	5.63e-5	—	5.63e-5	—	8.66e-4	—	5.59e+1	8.61e+2
$\kappa=1$										
N	MAC	rate	BCG exact	rate	BCG approx	rate	KM approx	rate	min ratio	max ratio
64	-9.41e-5	1.62	3.05e-3	0.82	3.05e-3	0.82	6.31e-3	0.35	3.25e+1	6.71e+1
128	-3.06e-5	1.75	1.73e-3	0.85	1.73e-3	0.85	4.94e-3	0.28	5.65e+1	1.61e+2
256	-9.08e-6	1.88	9.59e-4	0.92	9.59e-4	0.92	4.07e-3	0.23	1.06e+2	4.48e+2
512	-2.47e-6	—	5.07e-4	—	5.08e-4	—	3.46e-3	—	2.06e+2	1.40e+3
$\kappa=10$										
N	MAC	rate	BCG exact	rate	BCG approx	rate	KM approx	rate	min ratio	max ratio
64	-7.74e-4	0.88	2.06e-2	0.54	2.06e-2	0.54	3.07e-2	0.35	2.67e+1	3.97e+1
128	-4.20e-4	1.20	1.41e-2	0.74	1.41e-2	0.74	2.42e-2	0.39	3.37e+1	5.76e+1
256	-1.82e-4	1.18	8.47e-3	0.86	8.47e-3	0.86	1.85e-2	0.35	4.64e+1	1.01e+2
512	-8.04e-5	—	4.68e-3	—	4.68e-3	—	1.45e-2	—	5.82e+1	1.80e+2
$\kappa=100$										
N	MAC	rate	BCG exact	rate	BCG approx	rate	KM approx	rate	min ratio	max ratio
64	-4.77e-4	-0.71	1.11e-1	0.09	1.11e-1	0.09	1.41e-1	0.07	2.33e+2	2.95e+2
128	-7.81e-4	0.12	1.04e-1	0.49	1.04e-1	0.49	1.34e-1	0.36	1.34e+2	1.72e+2
256	-7.21e-4	1.27	7.42e-2	0.73	7.42e-2	0.73	1.05e-1	0.47	1.03e+2	1.45e+2
512	-3.00e-4	—	4.47e-2	—	4.47e-2	—	7.54e-2	—	1.49e+2	2.52e+2

by the cell-centered schemes, and these differences appear to increase with increases in the elastic stiffness coefficient. The rates of area change of the staggered discretization are also one to two orders of magnitude smaller than those of the collocated discretizations, although in this case, there is a less clear relationship between the relative performance of the discretizations and the stiffness of the elastic structure.

4.2.2 Elastic shell composed of circumferential fibers

Our next set of tests uses the nonequilibrium configuration of the thick elastic shell composed of circumferential fibers. Upon release at the beginning of the simulations, the elastic body undergoes damped oscillations. We empirically determined that the dura-

Table 9: Maximum percent area loss (gain) for the dynamic elastic-shell test of Section 4.2.2 with $\nu=1.0e-2$. The maximum percent area loss (gain) is reported for $N=64, 128, 256,$ and 512 for the staggered-grid (MAC), cell-centered pressure-increment exact projection (BCG-exact), cell-centered pressure-increment approximate projection (BCG-approx), and cell-centered pressure-free approximate projection (KM-approx) solvers. The minimum and maximum ratios of the cell-centered and staggered-grid results for each value of N are reported in the right two columns. For this test, the discrepancies between the solution methods are relatively small, although the staggered-grid scheme still yields at least modestly improved volume conservation compared to the collocated discretizations.

$\nu=1.0e-2$											
$\kappa=0.1$											
N	MAC	rate	BCG exact	rate	BCG approx	rate	KM approx	rate	min ratio	max ratio	
64	-3.50e-2	1.78	-1.28e-1	1.75	-1.28e-1	1.75	1.17e+0	1.97	3.67e+0	3.35e+1	
128	-1.02e-2	1.88	-3.83e-2	1.85	-3.83e-2	1.85	3.00e-1	2.06	3.76e+0	2.94e+1	
256	-2.78e-3	1.95	-1.06e-2	1.92	-1.06e-2	1.92	7.18e-2	2.13	3.83e+0	2.59e+1	
512	-7.20e-4	—	-2.80e-3	—	-2.80e-3	—	1.64e-2	—	3.89e+0	2.27e+1	
$\kappa=1$											
N	MAC	rate	BCG exact	rate	BCG approx	rate	KM approx	rate	min ratio	max ratio	
64	-7.97e-2	1.63	-2.94e-1	1.67	-2.94e-1	1.67	1.07e+0	2.00	3.69e+0	1.35e+1	
128	-2.58e-2	1.78	-9.22e-2	1.73	-9.22e-2	1.73	2.70e-1	2.10	3.58e+0	1.05e+1	
256	-7.50e-3	1.88	-2.77e-2	1.83	-2.77e-2	1.83	6.28e-2	2.15	3.70e+0	8.36e+0	
512	-2.04e-3	—	-7.83e-3	—	-7.83e-3	—	1.41e-2	—	3.83e+0	6.90e+0	
$\kappa=10$											
N	MAC	rate	BCG exact	rate	BCG approx	rate	KM approx	rate	min ratio	max ratio	
64	-1.40e-1	1.39	-4.79e-1	1.38	-4.79e-1	1.38	9.39e-1	2.22	3.41e+0	6.68e+0	
128	-5.37e-2	1.64	-1.83e-1	1.57	-1.83e-1	1.57	2.01e-1	2.57	3.42e+0	3.75e+0	
256	-1.72e-2	1.78	-6.16e-2	1.73	-6.16e-2	1.73	3.40e-2	2.02	1.97e+0	3.57e+0	
512	-5.00e-3	—	-1.86e-2	—	-1.86e-2	—	-8.39e-3	—	1.68e+0	3.71e+0	
$\kappa=100$											
N	MAC	rate	BCG exact	rate	BCG approx	rate	KM approx	rate	min ratio	max ratio	
64	-1.93e-1	0.99	-6.33e-1	1.10	-6.34e-1	1.10	1.07e+0	2.84	3.27e+0	5.55e+0	
128	-9.73e-2	1.46	-2.96e-1	1.34	-2.96e-1	1.34	-1.50e-1	1.20	1.54e+0	3.05e+0	
256	-3.53e-2	1.66	-1.17e-1	1.55	-1.17e-1	1.55	-6.50e-2	1.56	1.84e+0	3.32e+0	
512	-1.11e-2	—	-4.00e-2	—	-4.00e-2	—	-2.20e-2	—	1.98e+0	3.59e+0	

tion of the first oscillation is approximately $\frac{3.125^{\log_{10}(\kappa)}}{\kappa} 0.703125$ for the range of boundary stiffnesses considered. We perform simulations similar to those of Section 4.1.2, except that here we allow the perturbed structure to undergo approximately three damped oscillations. Sample simulation results are shown in Fig. 4. Detailed results for $N=64, 128, 256,$ and 512 are reported in Tables 9 and 10 for $\nu=1.0e-2$ and for $\kappa=0.1, 1, 10,$ and 100 . All schemes appear to be converging at near second-order rates, and the differences in accuracy between the solution methods is relatively small. Nonetheless, the staggered-grid scheme still yields at least a modest improvement in total area conservation when compared to the collocated discretizations. In some cases, however, the rate of area change

Table 10: Rate of area loss (gain) for the dynamic elastic-shell test of Section 4.2.2 with $\nu=1.0e-2$. The rate of area loss (gain) is reported for $N=64, 128, 256,$ and 512 for the staggered-grid (MAC), cell-centered pressure-increment exact projection (BCG-exact), cell-centered pressure-increment approximate projection (BCG-approx), and cell-centered pressure-free approximate projection (KM-approx) solvers. The minimum and maximum ratios of the cell-centered and staggered-grid results for each value of N are reported in the right two columns. For this test, the discrepancies between the solution methods are relatively small, although the staggered-grid scheme still yields at least modestly improved volume conservation compared to the collocated discretizations except for the largest value of the elastic stiffness κ , for which the pressure-free approximate projection method can yield rates of area change that are smaller than those produced by the staggered-grid method.

$\nu=1.0e-2$										
$\kappa=0.1$										
N	MAC	rate	BCG exact	rate	BCG approx	rate	KM approx	rate	min ratio	max ratio
64	-1.05e-4	0.89	-2.16e-4	0.65	-2.16e-4	0.65	5.98e-3	1.01	2.06e+0	5.72e+1
128	-5.65e-5	0.92	-1.38e-4	0.64	-1.38e-4	0.64	2.96e-3	1.08	2.44e+0	5.24e+1
256	-2.99e-5	0.98	-8.84e-5	0.81	-8.84e-5	0.81	1.40e-3	1.13	2.95e+0	4.68e+1
512	-1.52e-5	—	-5.05e-5	—	-5.05e-5	—	6.38e-4	—	3.32e+0	4.20e+1
$\kappa=1$										
N	MAC	rate	BCG exact	rate	BCG approx	rate	KM approx	rate	min ratio	max ratio
64	-7.92e-4	0.61	-1.69e-3	0.26	-1.69e-3	0.26	1.83e-2	1.02	2.13e+0	2.31e+1
128	-5.19e-4	0.78	-1.41e-3	0.55	-1.41e-3	0.55	8.99e-3	1.10	2.72e+0	1.73e+1
256	-3.02e-4	0.86	-9.63e-4	0.72	-9.63e-4	0.72	4.20e-3	1.14	3.19e+0	1.39e+1
512	-1.66e-4	—	-5.84e-4	—	-5.84e-4	—	1.91e-3	—	3.52e+0	1.15e+1
$\kappa=10$										
N	MAC	rate	BCG exact	rate	BCG approx	rate	KM approx	rate	min ratio	max ratio
64	-5.41e-3	0.39	-1.16e-2	-0.04	-1.16e-2	-0.04	5.29e-2	1.20	2.15e+0	9.78e+0
128	-4.14e-3	0.65	-1.19e-2	0.45	-1.19e-2	0.45	2.31e-2	1.42	2.88e+0	5.57e+0
256	-2.64e-3	0.78	-8.71e-3	0.66	-8.71e-3	0.66	8.62e-3	1.51	3.26e+0	3.29e+0
512	-1.54e-3	—	-5.51e-3	—	-5.51e-3	—	3.02e-3	—	1.96e+0	3.58e+0
$\kappa=100$										
N	MAC	rate	BCG exact	rate	BCG approx	rate	KM approx	rate	min ratio	max ratio
64	-2.55e-2	-0.07	-2.41e-2	-1.41	-2.41e-2	-1.41	1.99e-1	1.71	9.43e-1	7.80e+0
128	-2.68e-2	0.48	-6.38e-2	0.11	-6.39e-2	0.11	6.07e-2	4.94	2.27e+0	2.39e+0
256	-1.91e-2	0.69	-5.93e-2	0.51	-5.93e-2	0.51	1.98e-3	-2.65	1.03e-1	3.10e+0
512	-1.19e-2	—	-4.17e-2	—	-4.17e-2	—	-1.24e-2	—	1.05e+0	3.51e+0

produced by the pressure-free approximate projection method is modestly smaller than that of the other solution methods.

4.2.3 Elastic shell composed of circumferential and radial fibers

Our final set of tests uses the nonequilibrium configuration of the thick elastic shell composed of both circumferential and radial fibers. Upon release at the beginning of the simulations, the elastic body undergoes damped oscillations. We empirically determined that the duration of the first oscillation is approximately $\frac{2.75^{\log_{10}(\kappa)}}{\kappa} 1.40625$ for the range

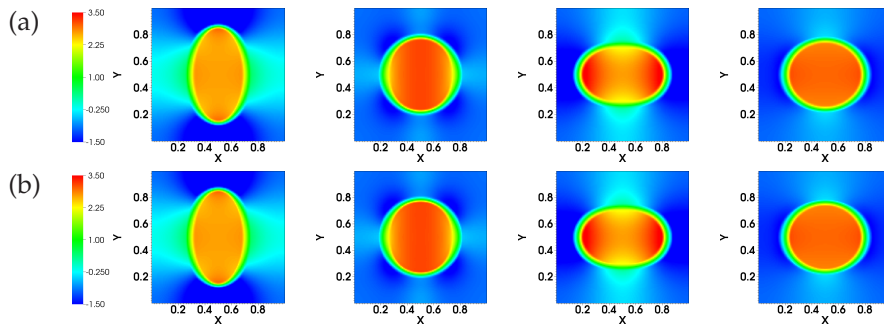


Figure 4: Results from the dynamic elastic shell test of Section 4.2.2. The top panels (a) show the pressure generated by the staggered-grid scheme at equally spaced time intervals during the first oscillation. The bottom panels (b) show the corresponding pressures generated by the pressure-increment approximate projection method. In both cases, $N=128$, $\nu=1.0e-2$, and $\kappa=1$.

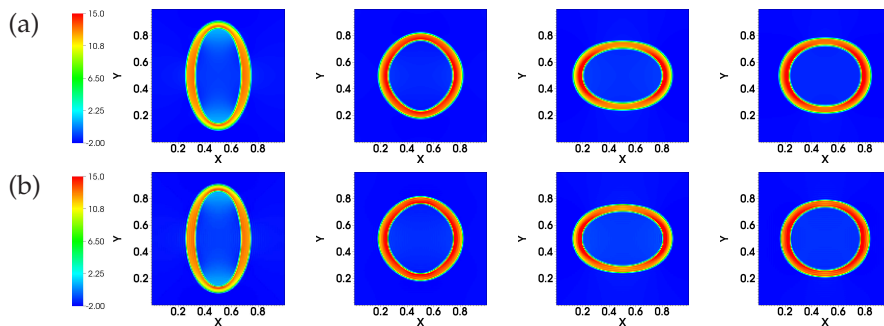


Figure 5: Results from the dynamic elastic shell test of Section 4.2.3. The top panels (a) show the pressure generated by the staggered-grid scheme at equally spaced time intervals during the first oscillation. The bottom panels (b) show the corresponding pressures generated by the pressure-increment approximate projection method. In both cases, $N=128$, $\nu=1.0e-2$, and $\kappa=1$.

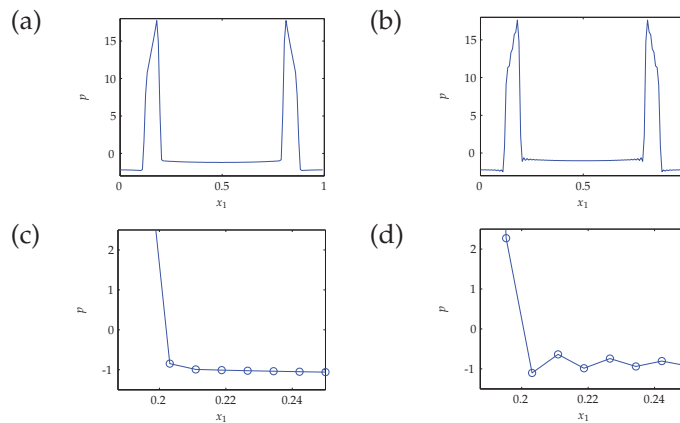


Figure 6: Pressure along $x_2=0.5$ for the staggered-grid (a and c) and pressure-increment approximate projection (b and d) IB methods for the dynamic thin-interface test of Section 4.2.3. Although both schemes regularize discontinuities in the pressure, notice the comparatively sharp resolution of the pressure discontinuity produced by the staggered-grid scheme. By contrast, the collocated scheme generates significant nonphysical pressure oscillations in the vicinity of such discontinuities.

Table 11: Maximum percent area loss for the dynamic elastic-shell test of Section 4.2.3 with $\nu=1.0e-2$. The maximum percent area loss is reported for $N=64, 128, \text{ and } 256$ for the staggered-grid (MAC), cell-centered pressure-increment exact projection (BCG-exact), cell-centered pressure-increment approximate projection (BCG-approx), and cell-centered pressure-free approximate projection (KM-approx) solvers. The minimum and maximum ratios of the cell-centered and staggered-grid results for each value of N are reported in the right two columns. In this case, the staggered-grid scheme yields area losses that are generally at least a factor of 5-20 smaller than those produced by the collocated schemes. The differences between the schemes appear to decrease with increasing elastic stiffness. Notice also that the pressure-free projection scheme yields unacceptably large area losses for all grid spacings considered.

$\nu=1.0e-2$										
$\kappa=0.1$										
N	MAC	rate	BCG exact	rate	BCG approx	rate	KM approx	rate	min ratio	max ratio
64	3.04e-1	0.84	5.24e+0	1.01	5.29e+0	1.01	9.43e+1	-0.03	1.72e+1	3.10e+2
128	1.70e-1	0.91	2.61e+0	1.02	2.63e+0	1.01	9.62e+1	0.24	1.53e+1	5.65e+2
256	9.03e-2	0.94	1.28e+0	0.99	1.30e+0	0.97	8.17e+1	0.68	1.42e+1	9.04e+2
512	4.70e-2	—	6.48e-1	—	6.66e-1	—	5.10e+1	—	1.38e+1	1.09e+3
$\kappa=1$										
N	MAC	rate	BCG exact	rate	BCG approx	rate	KM approx	rate	min ratio	max ratio
64	6.52e-1	0.95	7.99e+0	1.05	8.02e+0	1.05	9.45e+1	-0.02	1.23e+1	1.45e+2
128	3.37e-1	0.91	3.86e+0	1.03	3.88e+0	1.02	9.58e+1	0.31	1.14e+1	2.84e+2
256	1.80e-1	0.95	1.90e+0	1.00	1.92e+0	0.98	7.73e+1	0.59	1.05e+1	4.29e+2
512	9.33e-2	—	9.49e-1	—	9.75e-1	—	5.14e+1	—	1.02e+1	5.51e+2
$\kappa=10$										
N	MAC	rate	BCG exact	rate	BCG approx	rate	KM approx	rate	min ratio	max ratio
64	1.08e+0	0.85	1.09e+1	1.05	1.09e+1	1.05	9.47e+1	0.00	1.01e+1	8.77e+1
128	5.98e-1	0.92	5.25e+0	1.03	5.27e+0	1.03	9.44e+1	0.45	8.77e+0	1.58e+2
256	3.15e-1	0.94	2.56e+0	1.00	2.58e+0	0.98	6.89e+1	0.54	8.12e+0	2.18e+2
512	1.65e-1	—	1.28e+0	—	1.31e+0	—	4.74e+1	—	7.79e+0	2.88e+2
$\kappa=100$										
N	MAC	rate	BCG exact	rate	BCG approx	rate	KM approx	rate	min ratio	max ratio
64	1.48e+0	0.78	1.30e+1	1.07	1.30e+1	1.07	9.49e+1	0.06	8.75e+0	6.39e+1
128	8.67e-1	0.84	6.18e+0	1.06	6.19e+0	1.05	9.13e+1	0.59	7.13e+0	1.05e+2
256	4.84e-1	0.88	2.97e+0	0.99	2.99e+0	0.98	6.08e+1	0.52	6.15e+0	1.26e+2
512	2.62e-1	—	1.50e+0	—	1.51e+0	—	4.24e+1	—	5.72e+0	1.62e+2

of boundary stiffnesses considered. We perform simulations similar to those of Section 4.1.3, except that here we allow the perturbed structure to undergo approximately three damped oscillations. Sample simulation results are shown in Figs. 5 and 6. Detailed results for $N=64, 128, 256, \text{ and } 512$ are reported in Tables 11 and 12 for $\nu=1.0e-2$ and for $\kappa=0.1, 1, 10, \text{ and } 100$. As was the case in the corresponding quasi-static tests, the pressure-free approximate projection method yields extremely poor volume conservation for this test, with area losses of over 90% in many cases. The volume conservation of the other methods is comparatively good, especially the staggered-grid scheme, which yields area losses of less than 1% in many cases, even at very large elastic stiffnesses.

Table 12: Rate of area loss for the dynamic elastic-shell test of Section 4.2.3 with $\nu=1.0e-2$. The rate of area loss is reported for $N=64, 128, 256,$ and 512 for the staggered-grid (MAC), cell-centered pressure-increment exact projection (BCG-exact), cell-centered pressure-increment approximate projection (BCG-approx), and cell-centered pressure-free approximate projection (KM-approx) solvers. The minimum and maximum ratios of the cell-centered and staggered-grid results for each value of N are reported in the right two columns. In this case, the staggered-grid scheme yields rates of area loss that are generally at least a factor of 5-10 smaller than those produced by the collocated schemes. The differences between the schemes appear to decrease with increasing elastic stiffness.

$\nu=1.0e-2$										
$\kappa=0.1$										
N	MAC	rate	BCG exact	rate	BCG approx	rate	KM approx	rate	min ratio	max ratio
64	2.25e-5	0.81	3.04e-4	0.98	3.04e-4	0.99	4.85e-3	-0.50	1.35e+1	2.15e+2
128	1.29e-5	0.92	1.54e-4	1.09	1.54e-4	1.08	6.88e-3	0.29	1.19e+1	5.34e+2
256	6.79e-6	0.94	7.24e-5	0.99	7.26e-5	0.99	5.64e-3	0.73	1.07e+1	8.30e+2
512	3.54e-6	—	3.64e-5	—	3.67e-5	—	3.40e-3	—	1.03e+1	9.63e+2
$\kappa=1$										
N	MAC	rate	BCG exact	rate	BCG approx	rate	KM approx	rate	min ratio	max ratio
64	1.76e-4	0.95	1.65e-3	1.13	1.65e-3	1.13	1.88e-2	-0.43	9.36e+0	1.07e+2
128	9.11e-5	0.91	7.54e-4	1.07	7.55e-4	1.06	2.54e-2	0.40	8.28e+0	2.79e+2
256	4.84e-5	0.95	3.59e-4	1.01	3.61e-4	1.00	1.92e-2	0.63	7.43e+0	3.96e+2
512	2.50e-5	—	1.78e-4	—	1.80e-4	—	1.24e-2	—	7.12e+0	4.96e+2
$\kappa=10$										
N	MAC	rate	BCG exact	rate	BCG approx	rate	KM approx	rate	min ratio	max ratio
64	1.06e-3	0.89	8.05e-3	1.18	8.03e-3	1.18	7.45e-2	-0.31	7.60e+0	7.05e+1
128	5.69e-4	0.95	3.54e-3	1.09	3.55e-3	1.08	9.23e-2	0.59	6.23e+0	1.62e+2
256	2.95e-4	0.95	1.67e-3	1.02	1.68e-3	1.00	6.15e-2	0.56	5.66e+0	2.08e+2
512	1.53e-4	—	8.25e-4	—	8.38e-4	—	4.16e-2	—	5.39e+0	2.72e+2
$\kappa=100$										
N	MAC	rate	BCG exact	rate	BCG approx	rate	KM approx	rate	min ratio	max ratio
64	5.37e-3	0.89	3.55e-2	1.28	3.53e-2	1.27	2.96e-1	-0.13	6.58e+0	5.52e+1
128	2.90e-3	0.89	1.46e-2	1.14	1.46e-2	1.14	3.23e-1	0.74	5.05e+0	1.11e+2
256	1.56e-3	0.90	6.63e-3	1.03	6.66e-3	1.02	1.94e-1	0.52	4.25e+0	1.24e+2
512	8.36e-4	—	3.25e-3	—	3.29e-3	—	1.35e-1	—	3.89e+0	1.61e+2

5 Conclusions

In this paper, we have presented empirical tests that examine the volume-conservation properties of the IB method for several choices of Eulerian discretization and solution methods. Our tests considered a broad range of boundary stiffnesses both for quasi-static problems and also for dynamic problems at moderate-to-high Reynolds numbers. For benchmark problems involving sharp discontinuities in the pressure, we found that the spurious volume changes exhibited by the staggered-grid scheme are generally more than an order of magnitude smaller than those of the collocated solution methods. For problems that do not include such discontinuities, there is a smaller difference in the

volume-conservation properties of the schemes, although the staggered-grid discretization still generally yields modestly improved volume conservation in comparison to the collocated schemes in such cases. We believe that these differences between collocated and staggered-grid IB schemes are not well appreciated by the IB community, and we hope these empirical observations will be useful to those who use the IB method and who wish to improve the accuracy of IB or IB-like methods. At present, a theoretical explanation for the differences in volume-conservation between staggered and collocated IB methods is lacking, and a potentially important line of future research is to develop a more complete understanding of the differences.

A possible route to improve further the volume conservation of the staggered-grid IB method might be to employ a divergence-preserving interpolation scheme, like that of Tóth and Roe [41], which ensures that the continuous divergence of the interpolated velocity field in the interior of each Cartesian grid cell is equal to the discrete divergence of the staggered-grid velocity field within that cell. (No such interpolation scheme appears to exist for collocated velocity fields, be they cell- or node-centered.) One potential difficulty of using the interpolation scheme of Tóth and Roe in the context of the IB method is that this scheme yields an interpolated velocity field that is not continuous at the boundaries between the Cartesian grid cells. Consequently, the Lagrangian velocity field would possess apparent mass sources or sinks at these boundaries, and therefore would not yield exact discrete volume conservation in general. Further, it is generally thought to be important to advect the curvilinear mesh nodes by a continuous Lagrangian velocity field [1], e.g., to prevent nonphysical self-intersections of the immersed boundary. Nonetheless, it seems worthwhile to investigate interpolation schemes that attempt to exploit the structure of the staggered-grid velocity field.

We also considered the effect on volume conservation of using cell-centered approximate projection methods with the IB method. We found that the form of the approximate projection method has a large impact on the volume-conservation properties of the scheme. Pressure-free approximate projection methods, in which no approximation to the pressure gradient is included in the approximation to the momentum equation, were found to yield extremely poor volume conservation for certain problems. By contrast, the volume conservation of pressure-increment approximate projection methods, in which a time step-lagged approximation to the pressure gradient is included when solving the momentum equation, is similar to that of cell-centered exact projection IB methods. Consequently, for problems in which a collocated IB method yields adequate volume conservation, as may be the case at lower Reynolds numbers, the accuracy yielded by an appropriate approximate projection IB method may be comparable to that of a more expensive exact-projection IB method.

One limitation of this study is that we have not considered collocated discretizations that define approximations to the pressure and velocity at different spatial locations, e.g., the scheme of Almgren et al. [16], which employs a cell-centered discretization of the velocity and a node-centered discretization of the pressure. Such schemes might offer improved volume conservation compared to purely cell-centered or purely node-centered

discretizations, and they appear to be more straightforward to extend to adaptively refined Cartesian grids [17] than staggered-grid Eulerian discretizations. An advantage of the staggered-grid Eulerian discretization, however, is that it is stable and does not suffer from spurious pressure modes that can lead to nonphysical instabilities, especially for problems involving singular forcing terms.

A second limitation of this study is that we have not included a direct comparison to the improved volume conservation IB method of Peskin and Printz [2]. We remark, however, that Peskin and Printz report improvements in volume conservation that are quantitatively similar to the difference between staggered-grid and collocated discretizations demonstrated in the present work. It may be possible to follow their approach to derive modified staggered-grid finite-difference operators that further improve the volume-conservation properties of the staggered-grid IB method. We anticipate, however, that the unmodified staggered-grid approach will prove more useful in practice both because it is likely to be easier to implement and also because its extensions to cases involving adaptive mesh refinement [23, 25, 26, 28, 29] or physical boundary conditions [25, 27, 29] are significantly more straightforward. Such extensions, which we and others are actively developing, are needed in the context of many of the applications of the IB method to challenging problems of fluid-structure interaction.

Acknowledgments

We gratefully acknowledge research support from American Heart Association grant 10SDG4320049 and National Science Foundation grants DMS 1016554 and OCI 1047734. We thank Charles S. Peskin for the argument that the advection velocity field used in the staggered-grid scheme is discretely divergence free. Computations were performed at New York University using computer facilities funded in large part by a generous donation by St. Jude Medical, Inc.

References

- [1] C. S. Peskin. The immersed boundary method. *Acta Numer.*, 11: 479–517, 2002.
- [2] C. S. Peskin and B. F. Printz. Improved volume conservation in the computation of flows with immersed elastic boundaries. *J. Comput. Phys.*, 105(1): 33–46, 1993.
- [3] R. Cortez and M. L. Minion. The blob projection method for immersed boundary problems. *J. Comput. Phys.*, 161(2): 428–453, 2000.
- [4] Y. Kim and M.-C. Lai. Simulating the dynamics of inextensible vesicles by the penalty immersed boundary method. *J. Comput. Phys.*, 229(12): 4840–4853, 2010.
- [5] Y. Kim, M.-C. Lai, and C. S. Peskin. Numerical simulations of two-dimensional foam by the immersed boundary method. *J. Comput. Phys.*, 229(13): 5194–5207, 2010.
- [6] K. Shoele and Q. Zhu. Flow-induced vibrations of a deformable ring. *J. Fluid Mech.*, 650: 343–362, 2010.
- [7] E. P. Newren. Enhancing the immersed boundary method: stability, volume conservation, and implicit solvers. PhD thesis, University of Utah, 2007.

- [8] J. A. Stockie. Modelling and simulation of porous immersed boundaries. *Comput. Struct.*, 87(11–12): 701–709, 2009.
- [9] F. H. Harlow and J. E. Welch. Numerical calculation of time-dependent viscous incompressible flow of fluid with free surface. *Phys. Fluid*, 8(12): 2182–2189, 1965.
- [10] W. J. Rider, J. A. Greenough, and J. R. Kamm. Accurate monotonicity- and extrema-preserving methods through adaptive nonlinear hybridizations. *J. Comput. Phys.*, 225(2): 1827–1848, 2007.
- [11] P. Colella and P. R. Woodward. The piecewise parabolic method (PPM) for gas-dynamical simulations. *J. Comput. Phys.*, 54(1): 174–201, 1984.
- [12] A. J. Chorin. Numerical solution of the Navier-Stokes equations. *Math. Comput.*, 22(104): 745–762, 1968.
- [13] A. J. Chorin. On the convergence of discrete approximations to the Navier-Stokes equations. *Math. Comput.*, 23(106): 341–353, 1969.
- [14] J. Kim and P. Moin. Application of a fractional-step method to incompressible Navier-Stokes equations. *J. Comput. Phys.*, 59(2): 308–323, 1985.
- [15] J. B. Bell, P. Colella, and H. M. Glaz. A second-order projection method for the incompressible Navier-Stokes equations. *J. Comput. Phys.*, 85(2): 257–283, 1989.
- [16] A. S. Almgren, J. B. Bell, and W. G. Szymczak. A numerical method for the incompressible Navier-Stokes equations based on an approximate projection. *SIAM J. Sci. Comput.*, 17(2): 358–369, 1996.
- [17] A. S. Almgren, J. B. Bell, P. Colella, L. H. Howell, and M. L. Welcome. A conservative adaptive projection method for the variable density incompressible Navier-Stokes equations. *J. Comput. Phys.*, 142(1): 1–46, 1998.
- [18] A. S. Almgren, J. B. Bell, and W. Y. Crutchfield. Approximate projection methods: Part I. Inviscid analysis. *SIAM J. Sci. Comput.*, 22(4): 1139–1159, 2000.
- [19] D. F. Martin and P. Colella. A cell-centered adaptive projection method for the incompressible Euler equations. *J. Comput. Phys.*, 163(2): 271–312, 2000.
- [20] D. L. Brown, R. Cortez, and M. L. Minion. Accurate projection methods for the incompressible Navier-Stokes equations. *J. Comput. Phys.*, 168(2): 464–499, 2001.
- [21] D. F. Martin, P. Colella, and D. Graves. A cell-centered adaptive projection method for the incompressible Navier-Stokes equations in three dimensions. *J. Comput. Phys.*, 227(3): 1863–1886, 2008.
- [22] B. E. Griffith and C. S. Peskin. On the order of accuracy of the immersed boundary method: Higher order convergence rates for sufficiently smooth problems. *J. Comput. Phys.*, 208(1): 75–105, 2005.
- [23] B. E. Griffith, R. D. Hornung, D. M. McQueen, and C. S. Peskin. An adaptive, formally second order accurate version of the immersed boundary method. *J. Comput. Phys.*, 223(1): 10–49, 2007.
- [24] E. P. Newren, A. L. Fogelson, R. D. Guy, and R. M. Kirby. Unconditionally stable discretizations of the immersed boundary equations. *J. Comput. Phys.*, 222(2): 702–719, 2007.
- [25] B. E. Griffith, X. Luo, D. M. McQueen, and C. S. Peskin. Simulating the fluid dynamics of natural and prosthetic heart valves using the immersed boundary method. *Int. J. Appl. Mech.*, 1(1): 137–177, 2009.
- [26] B. E. Griffith, R. D. Hornung, D. M. McQueen, and C. S. Peskin. Parallel and adaptive simulation of cardiac fluid dynamics. In M. Parashar and X. Li, editors, *Advanced Computational Infrastructures for Parallel and Distributed Adaptive Applications*. John Wiley and Sons, Hoboken, NJ, USA, 2009.

- [27] B. E. Griffith. An accurate and efficient method for the incompressible Navier-Stokes equations using the projection method as a preconditioner. *J. Comput. Phys.*, 228(20): 7565–7595, 2009.
- [28] A. M. Roma, C. S. Peskin, and M. J. Berger. An adaptive version of the immersed boundary method. *J. Comput. Phys.*, 153(2): 509–534, 1999.
- [29] B. E. Griffith. Immersed boundary model of aortic heart valve dynamics with physiological driving and loading conditions. *Int. J. Numer. Meth. Biomed. Eng.*, To appear.
- [30] IBAMR: An adaptive and distributed-memory parallel implementation of the immersed boundary method. <http://ibamr.googlecode.com>.
- [31] SAMRAI: Structured Adaptive Mesh Refinement Application Infrastructure. <http://www.llnl.gov/CASC/SAMRAI>.
- [32] R. D. Hornung and S. R. Kohn. Managing application complexity in the SAMRAI object-oriented framework. *Concurrency Comput. Pract. Ex.*, 14(5): 347–368, 2002.
- [33] R. D. Hornung, A. M. Wissink, and S. R. Kohn. Managing complex data and geometry in parallel structured AMR applications. *Eng. Comput.*, 22(3–4): 181–195, 2006.
- [34] S. Balay, K. Buschelman, W. D. Gropp, D. Kaushik, M. G. Knepley, L. C. McInnes, B. F. Smith, and H. Zhang. PETSc Web page, 2009. <http://www.mcs.anl.gov/petsc>.
- [35] S. Balay, K. Buschelman, V. Eijkhout, W. D. Gropp, D. Kaushik, M. G. Knepley, L. C. McInnes, B. F. Smith, and H. Zhang. PETSc users manual. Technical Report ANL-95/11 - Revision 3.0.0, Argonne National Laboratory, 2008.
- [36] S. Balay, V. Eijkhout, W. D. Gropp, L. C. McInnes, and B. F. Smith. Efficient management of parallelism in object oriented numerical software libraries. In E. Arge, A. M. Bruaset, and H. P. Langtangen, editors, *Modern Software Tools in Scientific Computing*, pages 163–202. Birkhäuser Press, 1997.
- [37] *hypre*: High performance preconditioners. <http://www.llnl.gov/CASC/hypre>.
- [38] R. D. Falgout and U. M. Yang. *hypre*: a library of high performance preconditioners. In P. M. A. Sloot, C. J. K. Tan, J. J. Dongarra, and A. G. Hoekstra, editors, *Computational Science - ICCS 2002 Part III*, volume 2331 of *Lecture Notes in Computer Science*, pages 632–641. Springer-Verlag, 2002. Also available as LLNL Technical Report UCRL-JC-146175.
- [39] D. Boffi, L. Gastaldi, L. Heltai, and C. S. Peskin. On the hyper-elastic formulation of the immersed boundary method. *Comput. Meth. Appl. Mech. Engrg.*, 197(25–28): 2210–2231, 2008.
- [40] B. E. Griffith and X. Luo. Hybrid finite difference/finite element version of the immersed boundary method. Submitted, preprint available from <http://www.cims.nyu.edu/~griffith>.
- [41] G. Tóth and P. L. Roe. Divergence- and curl-preserving prolongation and restriction formulas. *J. Comput. Phys.*, 180(2): 736–750, 2002.